FERMILAB-THESIS-1999-34

A MEASUREMENT OF THE WIDTH OF THE W VECTOR BOSON IN PROTON-ANTIPROTON COLLISIONS AT $\sqrt{s} = 1.8\,\mathrm{TeV}$

A Thesis

Submitted to the Faculty

of

Purdue University

by

Adam Dean Hardman

In Partial Fulfillment of the

Requirements for the Degree

of

Doctor of Philosophy

August 1999

ACKNOWLEDGMENTS

I want to thank Art Garfinkel for his great help and guidance before and during my thesis research. I greatly enjoyed working for Daniela Bortoletto in the Silicon Microstrip Detector Lab at Purdue University.

There were many people at CDF, Fermilab, who were a great help to me. I would like to acknowledge especially Larry Nodulman, Mark Lancaster and Randy Keup. Many thanks also to Bill Ashmanskas, Mark Bailey, Virgil Barnes, Bill Carithers, James Done, Andrew Gordon, Chris Green, Todd Keaffaber, Young-Kee Kim, Mark Kruse, Jinbo Liu, Arnold Pompos, David Saltzberg, Andrew Scott, Stephan Van Den Brink, Bob Wagner, Barry Wicklund, Eric Wicklund and Steve Worm.

To Rinah and her family Raul, Nellie, Rosebelle, Richelle, Ricah and Ranelle, who have been like my family for part of my life in the United States, I love and thank you all.

To my Mother, Jodi, Troy and James, who have always been ready to talk and listen when I needed them, I love you all.

This work was supported by the U.S. Department of Energy and the Argonne National Laboratory.

TABLE OF CONTENTS

Page

Page

LIST OF TABLES

LIST OF FIGURES

Figure Page

ABSTRACT

Hardman, Adam Dean, Ph.D., Purdue University, August 1999. A Measurement of the Width of the W Vector Boson in Proton-Antiproton Collisions at $\sqrt{s} = 1.8\,\mathrm{TeV}$. Major Professor: Arthur Garfinkel.

This thesis describes a measurement of the W vector boson total width, Γ_W, from the tail of the W transverse mass distribution. The 90 pb^{-1} of data used in this thesis were collected by the Collider Detector at Fermilab (CDF) from $p\overline{p}$ collisions at a center-of-mass energy of $\sqrt{s} = 1.8\,\mathrm{TeV}$. Fitting a Monte Carlo simulation to the data over the W transverse mass distribution in the range $100\,\mathrm{GeV} < \mathrm{M_T} < 200\,\mathrm{GeV}$, we find that $\Gamma_W = 1.78^{+0.20}_{-0.19}(\mathrm{stat.}) \pm 0.14(\mathrm{syst.})\mathrm{GeV}$.

1. INTRODUCTION

The currently accepted theory of fundamental particle physics is called the Standard Model. The Standard model has not been challenged, as yet, by any experimental result. The Standard Model describes the strong and electroweak interactions between particles but not the much weaker gravitational interaction. The theory of strong interactions, or quantum chromodynamics (QCD), is not directly related to the measurement described in this thesis and so will not be discussed here. The electroweak interaction is a consequence of local gauge invariance under $SU(2)_L \times U(1)$, $SU(2)_L$ being the weak isospin group and $U(1)$ being the weak hypercharge group. The subscript L refers to the fact that the $SU(2)$ gauge symmetry is applied to left-handed fermion fields only. In this scheme, the elementary fermions are either in left handed weak isodoublets or right handed weak isosinglets:

$$\begin{pmatrix} u \\ d' \end{pmatrix}_L \quad \begin{pmatrix} c \\ s' \end{pmatrix}_L \quad \begin{pmatrix} t \\ b' \end{pmatrix}_L \qquad u_R \quad d_R \quad c_R \quad s_R \quad t_R \quad b_R$$

$$\begin{pmatrix} \nu_e \\ e^- \end{pmatrix}_L \quad \begin{pmatrix} \nu_\mu \\ \mu^- \end{pmatrix}_L \quad \begin{pmatrix} \nu_\tau \\ \tau^- \end{pmatrix}_L \qquad e_R^- \;\; \mu_R^- \;\; \tau_R^- \;\; \nu_{eR} \;\; \nu_{\mu R} \;\; \nu_{\tau R}$$

where the right-handed neutrinos are needed in case neutrinos are found to have a non-zero rest mass. The lower members of the quark doublets have primes on them to indicate that they are weak eigenstates, not mass eigenstates. The following equation shows the relationship between the weak eigenstates and the

mass eigenstates, where the (complex) transformation matrix, V, is known as the Cabibbo-Kobayashi-Maskawa (CKM) matrix:

$$\begin{pmatrix} d' \\ s' \\ b' \end{pmatrix} = V \begin{pmatrix} d \\ s \\ b \end{pmatrix}$$

$$V = \begin{pmatrix} V_{ud} & V_{us} & V_{ub} \\ V_{cd} & V_{cs} & V_{cb} \\ V_{td} & V_{ts} & V_{tb} \end{pmatrix}$$

This theory allows the existence of non-massive gauge bosons to carry the infinite-range electromagnetic interaction and massive gauge bosons to carry the short-range weak interaction. These bosons have been identified in experiments to be the massless photon (γ), and the massive $W^{\pm}$ and Z^0 particles.

The measurement of the total width of the W boson is the topic of this thesis. The rest of this chapter will discuss the theoretical prediction of the W width from the Standard Model and a summary of its previous experimental measurements.

1.1 A prediction of the W width

The Standard Model prediction of the partial width of the decay $W^+ \to \mu^+ \nu_\mu$ can be shown to be [1] :

$$, (W \to \mu\nu) = \frac{G_F M_W^3}{6\pi\sqrt{2}} \left(1 + \delta^{\mathrm{SM}}\right) = 226.0 \pm 0.8 \text{ MeV}$$

where $G_F = (1.16639 \pm 0.00002) \times 10^{-5}$ c^6/GeV^2 is the Fermi coupling constant, and $\delta^{\mathrm{SM}} = -0.0035 \pm 0.0017$ represents the oblique corrections to the tree level partial width. In this calculation [1] the world average of $M_W = 80.33 \pm 0.08$ GeV/c^2

was used. The W has essentially the same probability of decaying into each of the three lepton families and the two quark families that allow this kinematically. Each of the quark families have three different "colors" making six different decays into quarks possible: $[u\overline{d'}]_{R,B,G}$ and $[c\overline{s'}]_{R,B,G}$, where the subscript "R" represents red, "B" represents blue, and "G" represents green. These "colors" don't represent colors in the traditional sense, but represent a quantum mechanical property that differentiates the quarks from each other in the same manner that electric charge does. To a first approximation, then, the branching ratio of the $W \to \mu\nu$ is $\frac{1}{9}$. With Standard Model corrections, the full width is predicted [1] to be

$$, _W = 2.09 \pm 0.01 \text{ GeV}$$

1.2 Previous measurements of the W width

Several methods have been used to measure the W width. The measurable quantity R is defined

$$R = \frac{\sigma \cdot B(W \to l\nu)}{\sigma \cdot B(Z \to ll)}$$

where $\sigma \cdot B$ represents the cross section multiplied by branching ratio for each process. An alternative form for R can be written as:

$$R = \frac{\sigma(\overline{p}p \to WX)}{\sigma(\overline{p}p \to ZX)} \cdot \frac{, (W \to l\nu)}{, (Z \to ll)} \cdot \frac{, _Z}{, _W}$$

so that

$$, _W = \frac{1}{R} \cdot \frac{\sigma(W)}{\sigma(Z)} \cdot \frac{, _Z}{, (Z \to ll)} \cdot , (W \to l\nu)$$

The fraction $\frac{\sigma(W)}{\sigma(Z)}$ has been calculated theoretically [2], LEP has measured the value of $\frac{\Gamma(Z \to ll)}{\Gamma_Z}$ [3] and $, (W \to l\nu)$ has been calculated accurately by the Standard Model (see section 1.1), enabling the value of the W width to be extracted from a measurement of R. This method depends completely on Standard Model

theory, and its implicit theoretical uncertainties, and is hence called an "indirect" measurement of the W width. An alternative W width "indirect" measurement can be made by using the measured value of , $_Z$ and the Standard Model calculation of , $(Z \to ll)$, instead of the LEP measurement of the value of $\frac{\Gamma(Z \to ll)}{\Gamma_Z}$. Finally, it is possible to measure the W width directly from a fit to either the reconstructed W mass distribution, or by fitting the tail of W transverse mass distribution, the method to be used in this thesis. These "direct" methods are independent of the Standard Model, and can therefore be used as tests of the theory.

Table 1.1 shows the current status of W width measurements worldwide. Currently, the Particle Data Group [4] lists a world average value of , $_W = 2.06 \pm 0.06$ GeV. This value is still consistent with the Standard Model prediction given in the previous section meaning that Standard Model has not been challenged by the W width measurement at this time.

Table 1.1

Summary of previously published W width measurements. The first error given is statistical and the second is systematic. (D) refers to a direct measurement of the W transverse mass distribution, (E) refers to an extracted value from the measurement of $R = [\sigma(W)/\sigma(Z)]$[, $(W \rightarrow e\nu_e)$]/($B(Z \rightarrow ee)$, (W)), and (R) refers to a fit of the reconstructed W mass distribution.

Experiment	Reference	Decay channel	, (W) (GeV)
UA1-91	[5]	(E)	$2.18^{+0.26}_{-0.24} \pm 0.04$
UA2-92	[6]	(E)	$2.10^{+0.14}_{-0.13} \pm 0.09$
CDF-95	[7]	$W \rightarrow e\nu$ (D)	$2.11 \pm 0.28 \pm 0.16$
CDF-95	[8]	(E)	$2.064 \pm 0.060 \pm 0.059$
D0-95	[9]	(E)	2.044 ± 0.093
D0-99	[10]	(E)	$2.130 \pm 0.030 \pm 0.041$
L3-97	[11]	(R)	$1.74^{+0.88}_{-0.78} \pm 0.25$
OPAL-98	[12]	(R)	$1.30^{+0.70}_{-0.55} \pm 0.18$

2. THEORY

This chapter discusses the various decay modes of the W, the branching ratio for the $W \to \mu\nu$ in particular, the definition of the transverse mass, the form of the differential cross section for $W \to \mu\nu$ and an overview of the W width measurement method.

In $p\overline{p}$ collisions, W bosons are produced by processes of the type $u\overline{d} \to W^+$ and $\overline{u}d \to W^-$. They then decay either leptonically or hadronically in the following ways:

$$W^\pm \to e^+\nu_e,\ e^-\overline{\nu}_e$$

$$W^\pm \to \mu^+\nu_\mu,\ \mu^-\overline{\nu}_\mu$$

$$W^\pm \to \tau^+\nu_\tau,\ \tau^-\overline{\nu}_\tau$$

$$W^\pm \to q'\overline{q}$$

where q represents one of the quarks u, d, c, s, or b (but not t because it is heavier than the W). As given in section 1.1 the partial decay width for $W \to \mu\nu$ is

$$, (W \to \mu\nu) = \frac{G_F}{\sqrt{2}}\frac{M_W^3}{6\pi}\left(1+\delta^{\mathrm{SM}}\right) \equiv , {}^0_W \tag{2.1}$$

The e and τ leptons also have the same partial decay width. Under the assumption that the total hadronic decay rate is the same as the decay rate to quark-antiquark pairs, and that these quark-antiquark pairs fragment completely into hadrons, then the lepton and quark decay channels are related by

$$, (W \to e\nu) = , (W \to \mu\nu) = , (W \to \tau\nu) = , {}^0_W, \tag{2.2}$$

$$, (W \to q'\overline{q}) = 3|V_{qq'}|^2, \, {}^0_W, \tag{2.3}$$

where V is the Cabibbo-Kobayashi-Maskawa quark mixing matrix [13],

$$|V_{qq'}| = \begin{pmatrix} 0.9747 - 0.9759 & 0.218 - 0.224 & 0.002 - 0.005 \\ 0.218 - 0.224 & 0.9738 - 0.9752 & 0.032 - 0.048 \\ 0.004 - 0.015 & 0.030 - 0.048 & 0.9988 - 0.9995 \end{pmatrix} \tag{2.4}$$

and all fermion masses have been neglected compared to M_W. The fact that quarks can have one of three different colors is responsible for the factor of 3 given in the rate for quark-mode decay rate. Equation 2.3 can be summed over the kinematically allowable quark generations:

$$\sum_{q'q} , (W \to q'\overline{q}) = 3, \, {}^0_W \sum_{q'q} |V_{qq'}|^2 \simeq 3, \, {}^0_W \left[|V_{ud}|^2 + |V_{cs}|^2 \right] \simeq 6, \, {}^0_W$$

Thus in comparing hadrons to leptons

$$, (W \to \text{hadrons}) \simeq 2, (W \to \text{leptons})$$

Therefore the branching fraction of the W into $\mu\nu$ is approximately

$$B(W \to \mu\nu) \simeq \frac{, (W \to \mu\nu)}{, (W \to \text{all})} = \frac{1}{9}$$

which compares well with the world average [13] of $(10.6 \pm 0.7\%)$.

2.1 The cross section for W production and decay into the muon mode

The production and decay of a W in the muon mode is shown to lowest order in the Feynman diagram in figure 2.1. The quarks directly producing the W are identified generically as $\overline{q}_1$ and q_2 and the outgoing particles are shown with their usual identifying symbols. Although the quarks are constituents of a proton and antiproton which have equal and opposite momenta, the quarks themselves do

not have equal and opposite momenta, rather their momentum distributions are described by the relevant parton distribution functions. The diagram shown should only be considered a subprocess which needs to be summed over all quark species and weighted with the relevant parton distribution functions in order to obtain the total cross section for $p\overline{p} \to \mu\nu X$. Using the usual Feynman rules, the matrix element for this subprocess can be shown to be [14]:

$$\mathcal{M} = \frac{G_F}{\sqrt{2}} M_W^2 V_{q_1 q_2} \frac{\overline{v}(q_1)\gamma^\alpha(1-\gamma_5)u(q_2)\overline{u}(\nu)\gamma_\alpha(1-\gamma_5)v(\mu)}{\hat{s} - M_W^2 + i\hat{s},\ {}_W/M_W}$$

where G_F is the Fermi coupling constant, M_W and $,\ {}_W$ are the mass and width of the W, $V_{q_1 q_2}$ is an appropriate element of the CKM mixing matrix (Equation 2.4), $\hat{s}$ is the total energy squared in the subprocess center-of-mass-frame. The standard Dirac wave functions u and v, and γ matrix are also used in the above equation to obtain the spin sum

$$\sum_{spins} \overline{|\mathcal{M}|^2} = 4|V_{q_1 q_2}|^2 \left(\frac{G_F M_W^2}{\sqrt{2}}\right)^2 \frac{\hat{s}(1+\cos\hat{\theta})^2}{(\hat{s} - M_W^2)^2 + \hat{s}^2,\ {}_W^2/M_W^2}$$

Here $\hat{\theta}$ is the polar angle of the muon in the subprocess center of mass frame. From this, the differential cross section can be shown to be:

$$\frac{d\hat{\sigma}}{d\cos\hat{\theta}}(q_1 q_2 \to \mu\nu) = \frac{|V_{q_1 q_2}|^2}{8\pi} \left(\frac{G_F M_W^2}{\sqrt{2}}\right)^2 \frac{\hat{s}(1+\cos\hat{\theta})^2}{(\hat{s} - M_W^2)^2 + \hat{s}^2,\ {}_W^2/M_W^2}$$

and thus the total cross section is :

$$\hat{\sigma}(q_1 q_2 \to \mu\nu) = \frac{|V_{q_1 q_2}|^2}{3\pi} \left(\frac{G_F M_W^2}{\sqrt{2}}\right)^2 \frac{\hat{s}}{(\hat{s} - M_W^2)^2 + \hat{s}^2,\ {}_W^2/M_W^2}$$

The differential cross section depends on the total cross section in the following way :

$$\frac{d\hat{\sigma}}{d\cos\hat{\theta}}(q_1 q_2 \to \mu\nu) = \frac{3\hat{\sigma}}{8}(1+\cos\hat{\theta})^2$$

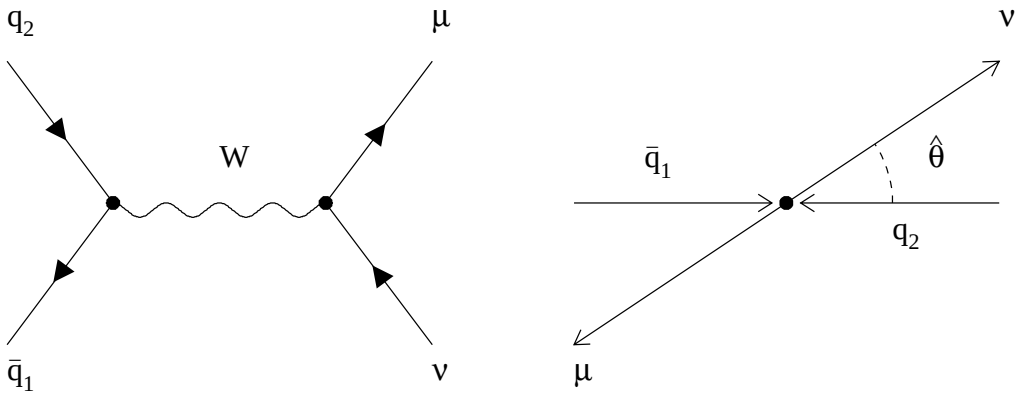

Figure 2.1

Feynman and center of momentum diagrams for lowest order W production.

Let us consider the cross section in terms of the muon momentum transverse* to the beam, p_T^μ. To the lowest order approximation, $p_T^\mu = p_T^\nu = \hat{p}_T$ where

$$\hat{p}_T^2 = \frac{1}{4}\hat{s}\sin^2\hat{\theta}$$

which leads to the differential cross section in terms of $\hat{p}_T$:

$$\frac{d\hat{\sigma}}{d\hat{p}_T^2} = \frac{\hat{\sigma}}{\hat{s}}\frac{3}{2}\frac{(1-2\hat{p}_T^2/\hat{s})}{(1-4\hat{p}_T^2/\hat{s})^{1/2}}$$

This form of the differential cross section is sharply peaked at $\hat{p}_T = \frac{1}{2}M_W$ and sensitive to M_W, hence it is a good candidate for finding M_W. When the $\mathcal{O}(\alpha_s)$ W production processes involving gluons are considered, however, the W acquires a non-zero transverse momentum. This property then causes the differential cross section to become smeared near the peak and thus gives rise to a loss in sensitivity

*The subscript T will always imply that we are referring to the component transverse to the beam.

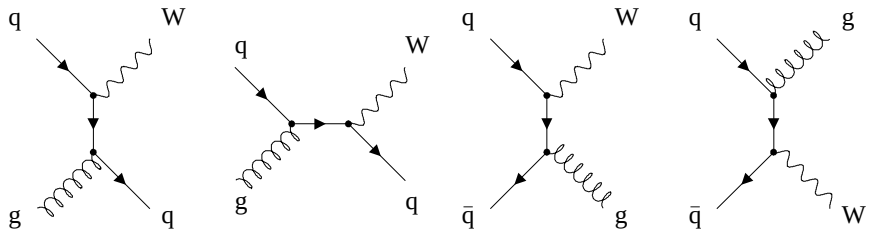

Figure 2.2

W production involving gluons.

to M_W. There are two types of gluon process, initial state gluon radiation and gluon Compton scattering, both types are shown in figure 2.2.

A quantity that is closer in meaning to M_W than $\hat{p}_T$ is the transverse mass of the muon-neutrino system, M_T, defined by (neglecting the muon mass)

$$M_T^2 \equiv (|\mathbf{p}_T^\mu| + |\mathbf{p}_T^\nu|)^2 - (\mathbf{p}_T^\mu + \mathbf{p}_T^\nu)^2 \tag{2.5}$$

Thus M_T takes on the range of values $0 \leq M_T \leq M_W$, the minimum being achieved when the muon and neutrino both move in the longitudinal direction, and the maximum being achieved when they both move in the transverse direction. When a Lorentz boost in the transverse plane is given to the W, then

$$M_T' = M_T + \mathcal{O}\left(\left[\frac{p_T^W}{E_T^W}\right]^2\right) + \ldots \tag{2.6}$$

$$p_T' = \hat{p}_T + \mathcal{O}\left(\frac{p_T^W}{E_T^W}\right) + \ldots \tag{2.7}$$

where E_T, the "transverse energy" of a particle, denotes the transverse component of the vector whose magnitude is the energy of the particle and direction is parallel to the momentum of the particle. These expressions show that M_T is less sensitive to p_T^W than p_T^μ is, which means it is advantageous to use as a fitting quantity, since the p_T^W distribution is not known accurately at present. It can be shown that the

M_T distribution has endpoints which are not affected by p_T boosts of the W, unlike the p_T^μ distributions.

Hence, we now would like to express the cross section in terms of M_T. In the approximation that p_T^W is small, $M_T = 2|\mathbf{p}_T^\mu| = 2|\mathbf{p}_T^\nu|$, and the following differential cross section is obtained :

$$\frac{d\hat{\sigma}}{dM_T^2} = \frac{\hat{\sigma}}{\hat{s}}\frac{3}{8}\frac{(2 - M_T^2/\hat{s})}{(1 - M_T^2/\hat{s})^{1/2}}$$

To transform to the lab frame, we need to sum over all the quark species and integrate over all quark momenta, while weighting the subprocess cross section with the appropriate parton distribution functions. This yields

$$d\sigma(p\overline{p} \to \mu\nu X) = \frac{K}{3}\sum_{q_1,q_2}\int_0^1 dx_1 \int_0^1 dx_2 q_1(x_1,\hat{s})q_2(x_2,\hat{s})d\hat{\sigma}(q_1q_2 \to \mu\nu)$$

The factor of 1/3 is due to averaging over initial quark colors, $K = 1 + \frac{8\pi}{9}\alpha_s(M_W^2)$ is a constant [14] that represents the correction for non-leading-order QCD effects, and $q_1(x_1,\hat{s})$ and $q_2(x_2,\hat{s})$ are the parton distribution functions evolved up to $Q^2 = \hat{s}$.

2.2 Finding the W width

The kinematic quantities (in the transverse plane) representing the final state particles in the process $p\overline{p} \to WX \to \mu\nu X$, where X represents the recoiling hadrons from the W, are shown in figure 2.3. The vector $\mathbf{u}$ represents the sum of the momentum of the hadrons due to the breakup of the proton and antiproton and the momentum of the hadrons due to the recoil against the W transverse momentum, and is called the recoil transverse energy vector. Thus we can see that the $\mathbf{p}_T^\nu$ in Equation 2.5 can be computed as

$$\mathbf{p}_T^\nu = -\mathbf{p}_T^\mu - \mathbf{u}$$

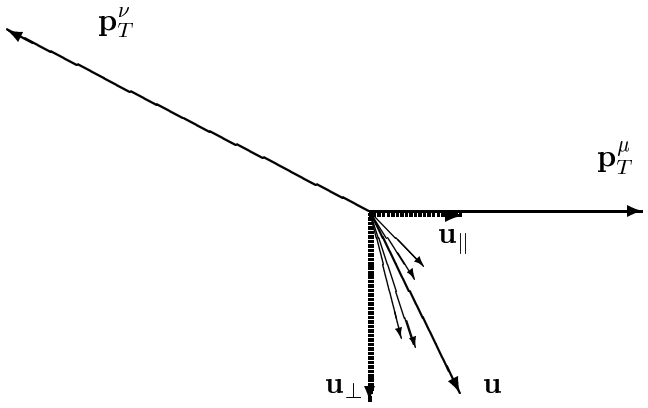

Figure 2.3

Kinematics of the final state products for the process $p\overline{p} \rightarrow WX \rightarrow \mu\nu X$, where X represents the recoiling hadrons from the W, as seen in the transverse plane to the beam.

Assuming $|\mathbf{u}| \ll p_T^{\mu}$ and using equation 2.5 we obtain:

$$M_T \approx 2p_T^{\mu} + u_{\parallel} \tag{2.8}$$

where the component of recoil transverse energy vector parallel to the muon momentum is defined $u_{\parallel} = (\mathbf{u} \cdot \mathbf{p}_T^{\mu})/p_T^{\mu}$. This expression shows that the muon transverse momentum and the parallel recoil transverse energy measurements are dominant in the determination of the transverse mass.

It has been theorized [14] that , $_W$ could be extracted from the data in the tail end of the M_T^W distribution from W production in $p\overline{p}$ collisions. Figure 2.4 shows Monte Carlo simulated M_T^W spectra, for a range of values of , $_W$. The plot shows the sensitivity of the tail end of the transverse mass distribution to the simulation , $_W$ value, particularly in the $100\,\text{GeV} < M_T^W < 200$ GeV region. In this region the detector resolution effects are minor because of their Gaussian type dependency

on the transverse mass. This is the region we will use to fit our Monte Carlo simulation to the data to extract a W width value.

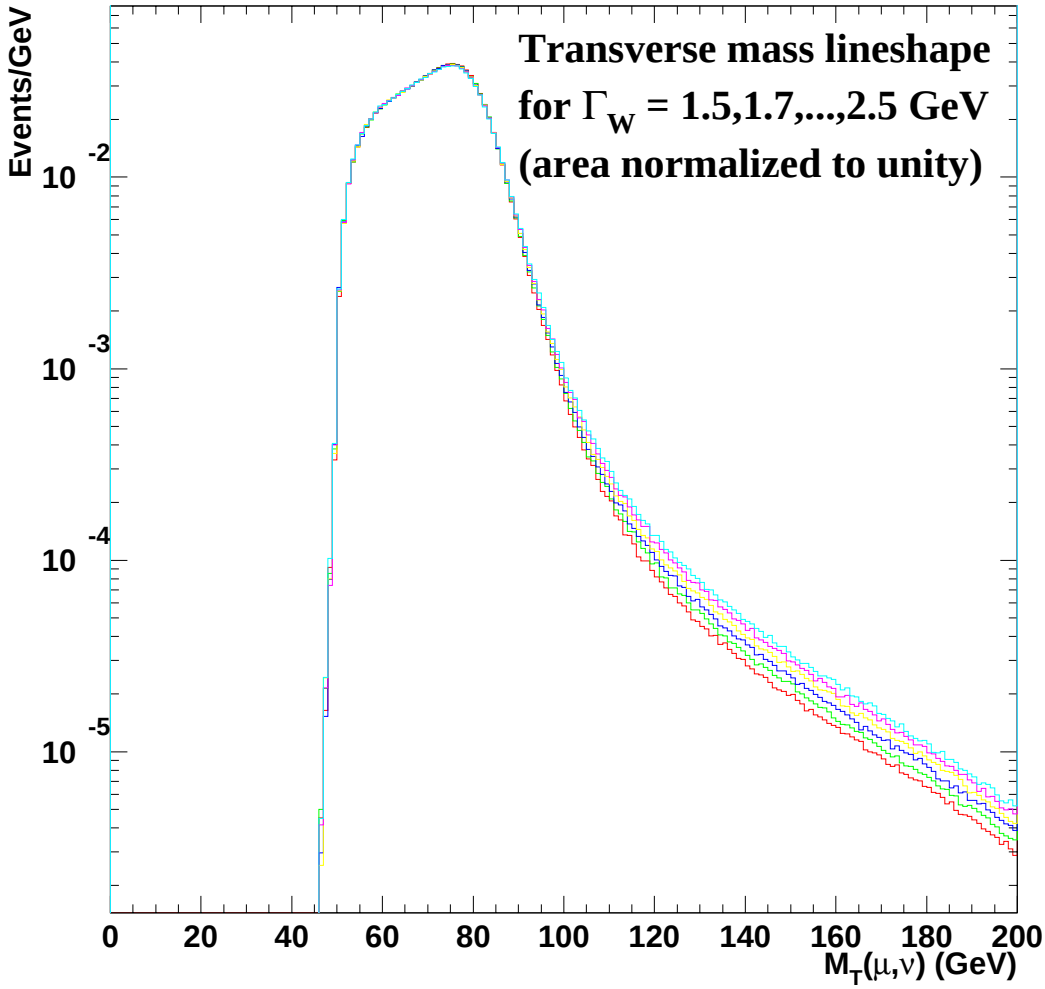

Figure 2.4

Sensitivity of W transverse mass distribution to , $_W$.

3. THE COLLIDER DETECTOR AT FERMILAB

At CDF, $p\overline{p}$ collisions (at $\sqrt{s} = 1.8$ TeV) with protons and antiprotons of equal and opposite momenta are used to produce W bosons. Most commonly the u/d quark from the proton collides with the $\overline{d}/\overline{u}$ quark from the antiproton to produce a W^+/W^-. The W produced decays very quickly in about 3×10^{-25} seconds, and its decay products enter into the CDF detector. This chapter describes the various components of the CDF detector at Fermilab.

3.1 Description of the CDF detector at the beginning of Run 1B

The CDF detector was built specifically to study $p\overline{p}$ collisions produced by the Fermilab Tevatron. It is an azimuthally* and forward-backward symmetric magnetic detector. The magnetic spectrometer part of the detector is composed of several tracking devices inside a 3-m diameter, 5-m long superconducting solenoidal magnet with a field of 1.4 T. The detector is partitioned into a central region ($30^\circ < \theta < 150^\circ$), end-plugs ($10^\circ < \theta < 30^\circ$, $150^\circ < \theta < 170^\circ$) which form the pole pieces for the solenoidal magnet, and forward/backward regions ($2^\circ < \theta < 10^\circ$, $170^\circ < \theta < 178^\circ$). Muon coverage is provided by muon chambers located outside the hadronic calorimeters in the central region, and by toroidal steel magnets and chambers on each end. See figure 3.1 and figure 3.2 for diagrams of the CDF detector.

*The z axis is defined to be the beam direction at CDF (positive is east)

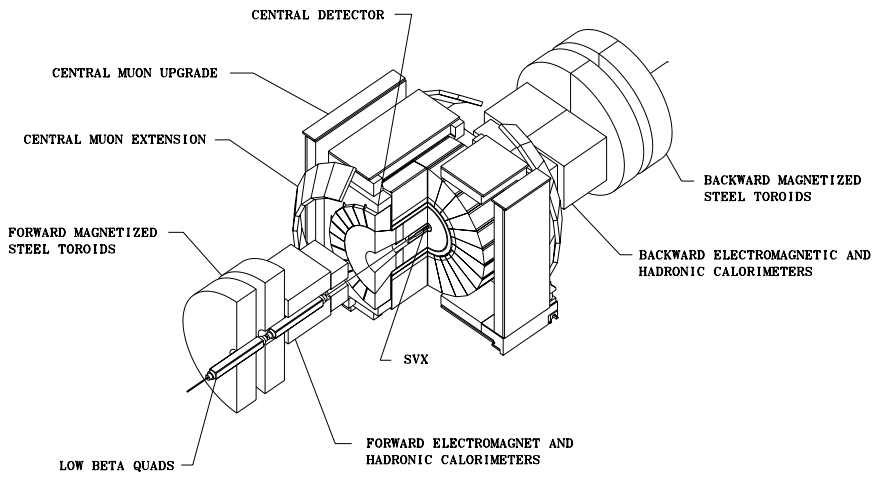

Figure 3.1

Isometric view of the CDF detector.

3.2 The Tracking Detectors

Tracking devices in the CDF magnetic spectrometer consist of; the silicon microstrip vertex detector (SVX′), the vertex time projection chambers system (VTX), and the central tracking chamber (CTC).

The four-layer silicon microstrip vertex detector (SVX′) consists of two adjacent barrels with axes along the beamline, one of which is shown in figure 3.3. It is used to accurately measure the position of the beam axis, a measurement that will later be used in the calculation of the momentum of the muon. The SVX′ is the innermost sensor of the CDF detector, the layers being located at radii of 3.0, 4.2,

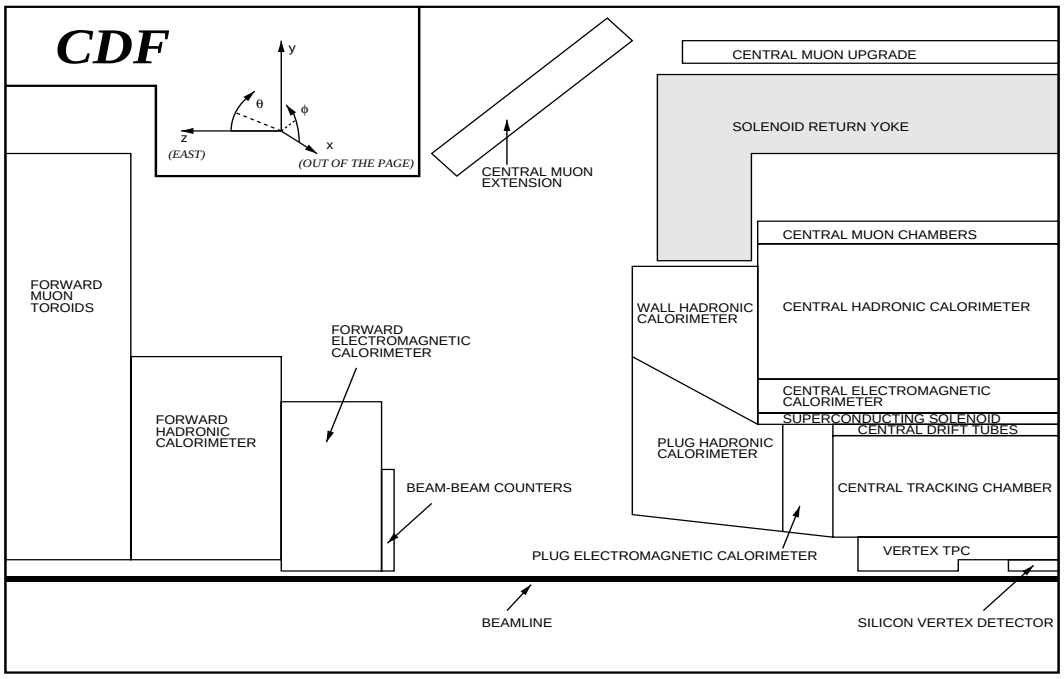

Figure 3.2

Cross section view of a side of the CDF detector with coordinate system defined.

5.7, and 7.9 cm from the beamline. The impact parameter resolution of the SVX′ has been measured to be 13 μm [15].

Just outside the SVX′ sits a group of vertex time projection chambers (VTX) which will be used to find the z position of the $p\overline{p}$ interaction (the event vertex) in this thesis. Event selection and muon track reconstruction rely critically on the location of the event vertex. The VTX has a z resolution of 200 μm at $\eta = 0$ (The pseudorapidity of a track, η, is defined as $\eta = -\ln(\tan(\theta/2))$).

The final tracking system is the central tracking chamber (CTC, see figure 3.4) which is used to measure the curvature, azimuthal angle and polar angle of tracks made by muons, in order to precisely determine their momenta. The CTC is a 321 cm long, 84-layer cylindrical drift chamber, covering a radius range of 31.0 to 132.5 cm. The CTC has 84 layers of sampling wires, which are divided into 9

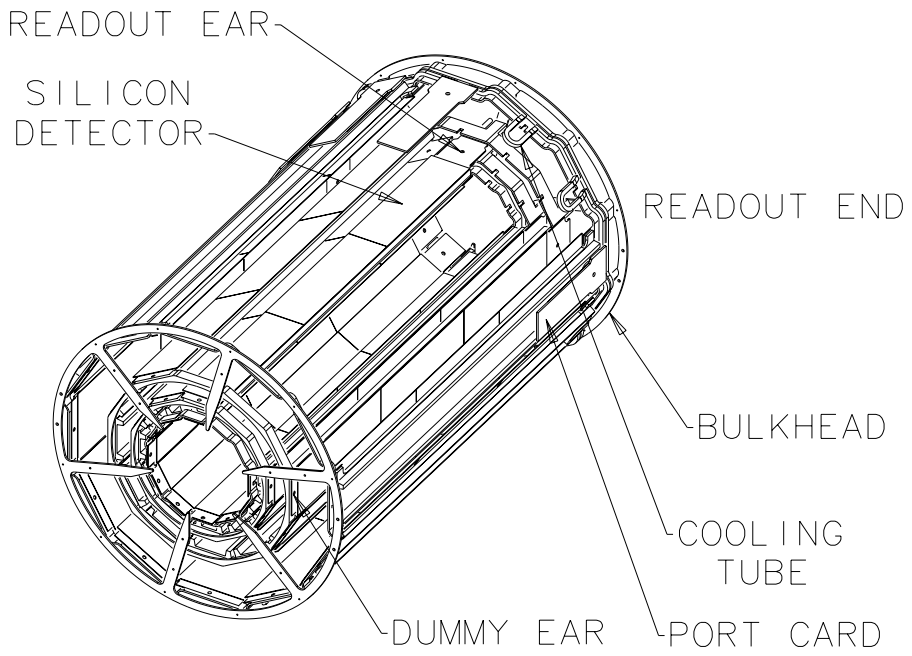

Figure 3.3

An SVX detector barrel. The SVX′ detector has a similar design.

radial regions called "super-layers". There are two classes of super-layers, the axial super-layers which consist of 12 radially separated layers of sense wires parallel to the z axis, and the stereo super-layers which consist of 6 radially separated layers of sense wires oriented with an approximately 3° stereo angle with respect to the z axis. This angle changes its sign for each successive stereo super-layer. The axial super-layers are used to measure the r-ϕ position of the track and the stereo super-layers are used to get a combination of r-ϕ and z information. Hence it is possible to gather enough information to form a three dimensional track from which to determine the momentum of a charged particle.

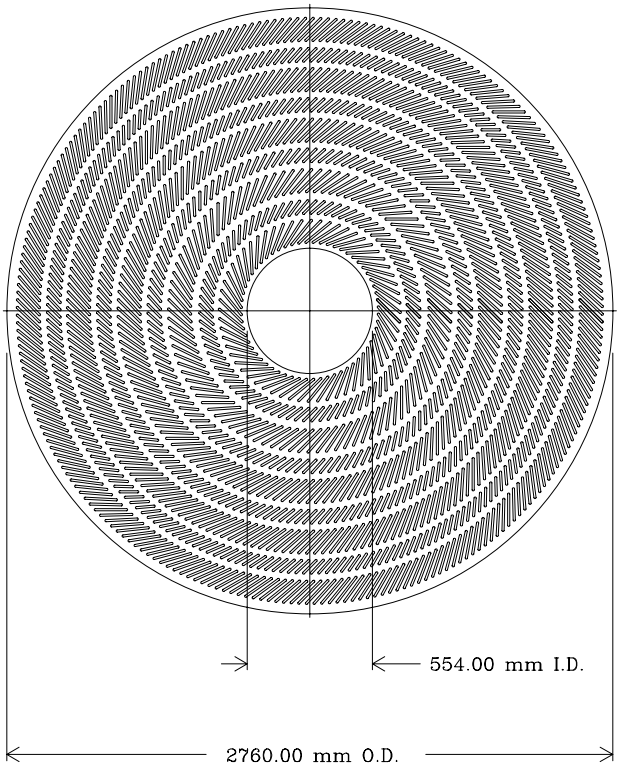

Figure 3.4

The CTC detector end plate.

3.3 The Calorimeters

There are two types of calorimeter in CDF, electromagnetic and hadronic. The electromagnetic calorimeters are generally used to identify and measure the energy of electrons and photons. Hadronic calorimeters measure hadronic energies and are useful in identifying muons. They subtend an angle of 2π in azimuth and cover the range -4.2 to 4.2 in pseudorapidity (η). A projective tower geometry (see figure 3.5) was used in the construction of the calorimeters, where the towers subtended approximately 0.1 in pseudorapidity and 15° in ϕ for the central calorimeters and 5° in ϕ for the plug and forward calorimeters. The hadronic

calorimeter for each tower is located at a larger radius than the corresponding electromagnetic calorimeter. The central calorimeter consists of 24 "wedges" in ϕ for a detector "half", the two halves being defined as $-1.1 < \eta < 0$ and $0 < \eta < 1.1$. Ten electromagnetic towers make up each wedge, each tower being composed of lead for the absorber and scintillators for the active medium. Hence, in total, there are 480 central electromagnetic calorimeter (CEM) towers. The electron shower position at a depth of approximately six radiation lengths (which is approximately the shower maximum for electromagnetic showers) in the CEM is measured in ϕ and z by a proportional chamber called the central electromagnetic strip detector (CES). The calibration of the CEM is done using the testbeam data taken during 1984-85.

The central calorimeters are used to measure the energy carried by the recoil particles resulting from W production. Since a fraction of these particles are hadrons, the central hadronic calorimeter (CHA) is needed. The CHA surrounds and is similarly segmented to the CEM. There are also other calorimeters which extend the range of η that can be covered, namely the PEM (Plug Electromagnetic Calorimeter), WHA (Wall Hadronic Calorimeter), PHA (Plug Hadronic Calorimeter), FEM (Forward Electromagnetic Calorimeter) and FHA (Forward Hadronic Calorimeter). The central calorimeters act as a hadron absorber for the central muon detection system, which will be discussed next.

3.4 The Muon Detectors

The outermost layers of the CDF detector are involved with muon detection. Data from three of these muon detectors are used in the muon W width measurement. The first is the central muon detector (CMU), which is located just outside the CHA, but within the same wedge as it. The CMU consists of four layers of

Figure 3.5

Cross section view of side of the CDF detector.

drift cells and provides a coverage of $|\eta| < 0.6$. The drift cell wires run parallel to the z axis and alternate layers in the $r - \phi$ plane have their centers aligned with the geometrical center of the detector. This allows the possibility of a rough momentum measurement of muons by the CMU. Muon tracks through the CMU are reconstructed by using charge division in the longitudinal (z) direction and time-to-distance relationships in the drift (ϕ) direction. Cosmic-ray studies [16] have shown that the drift direction has a resolution of 250 μm and the longitudinal direction (z) has a resolution of 1200 μm. Outside of the CMU are located 0.6 m thick steel absorbers, which in turn are surrounded by the four layers of drift chambers which make up the central muon upgrade detector (CMP). The muon detectors do not provide full azimuthal coverage however, the CMU covers about 84% of the solid angle, the CMP covers 63%, and they overlap for 53% of the solid angle. The third muon detector is the central muon extension detector (CMX) which is similar in chamber design to the CMP but on alternate layers the wire centers are collinear with the geometrical center of the detector. It extends over the pseudorapidity range $0.6 < |\eta| < 1.0$ and covers the azimuthal regions $0^\circ < \phi < 75^\circ$, $105^\circ < \phi < 225^\circ$ and $315^\circ < \phi < 360^\circ$.

4. DATA SAMPLE

The data used in this thesis were extracted from the 1994-1996 run at CDF. The integrated luminosity gathered over this period was 90 pb^{-1}. This chapter discusses the acquisition, calibrations and selection criteria applied to the raw data used to obtain a data sample with a high concentration of $W \to \mu\nu$ decays.

4.1 Trigger and Data Acquisition

The CDF trigger is organized into a three level system that chooses events for recording to magnetic tape. In the Tevatron, proton and antiproton bunches cross each other at a rate of 286 kHz, yielding a mean interaction rate of 3 interactions per crossing at a luminosity of $1.9 \times 10^{31} cm^{-2} sec^{-1}$. Dedicated electronic systems make up the first two levels of the trigger, each having separate data paths coming from the data readout system. After the event information is digitized and stored, the third level trigger then uses a farm of commercial computers to reconstruct the events.

The Level 1 muon trigger makes use of the drift times measured in the layers within the CMU chambers to calculate the angle made by the track with the radial lines that intersect the muon chamber wires. This angle is related to the transverse momentum and is hence used by the trigger to select high-p_T muons. For the Level 1 muon trigger, there is also the condition that if the track projects toward the CMP then there must exist a corresponding track through the CMP. At Level 2, the Central Fast Tracker (CFT) [17] uses CTC track information in the $r - \phi$

plane to look for hit patterns that indicate a high-p_T particle. The track for a low-p_T muon will be more curved than that of a high-p_T muon because of the axial magnetic field. The level-2 muon trigger compares the angle ϕ of tracks that the CFT accepts with the angle measured by the level 1 trigger. If the ϕ values differ by less than 5°, the event is passed onto the 3rd level trigger. Finally, at Level 3, reconstruction programs that include three-dimensional track reconstruction are used to identify high-p_T muons.

If an event is passed by the Level 3 trigger, then it is sorted and recorded. Rarer processes and interesting events (such as W decays), are written to disk in a separate data stream in addition to being recorded to magnetic tape with the bulk of events.

4.2 Reconstruction of Tracks in the CTC

The approximate relationship between transverse mass and transverse momentum, $M_T \approx 2p_T^{\mu} + u_{\parallel}$, shows the relative importance of the transverse momentum measurement.

The axial magnetic field in the CTC is close to being uniform (varies by about 1%). If the field were perfectly uniform, charged particles would leave hit patterns that followed helical trajectories. Mathematically, a helix can be parameterized by five quantities: curvature, c (inverse of the diameter of the circle in the $r-\phi$ plane); impact parameter, d_0 (distance of closest approach to $r = 0$)*; ϕ_0, (azimuthal angle of tangent to trajectory at point of closest approach to $r = 0$); z_0, (z coordinate at the point closest approach to $r = 0$); and $\cot\theta$, where θ is the polar angle of the trajectory.

*This is different from the quantity D_0 which will be used to refer to the distance of closest approach to the beam.

4.3 Calibration and Alignment in the CTC

Some corrections are needed to the track parameters of the muons we are interested in. These corrections come from studies of the processes $W \to e\nu$ and $J/\psi \to \mu\mu$.

The following correction is made to the magnitude of the momentum to account for the CTC cylinder axis not being quite parallel with the B-field axis [18]:

$$|\mathbf{p}|_{\text{corrected}} = |\mathbf{p}|[1 - 0.0017\cot\theta\sin(\phi - 1.9)]$$

Corrections derived from the studies of $W \to e\nu$ by Larry Nodulman [19], Bill Askmanskas and Aseet Mukherjee [20] are made to the muon kinematic variables of the above data sample (q is the sign of the charge of the muon) to account for false curvature effects in the CTC:

$$\left(\frac{1}{p_T}\right)_{\text{corrected}} = \frac{1}{p_T} - 0.00031q\sin(\phi - 3.0)$$

This correction is caused by the SVX$'$ measuring a different beam position to that from the CTC (also known as the "non-residual B-field correction").

A correction to the track parameter $\cot\theta$ was also found that, although it doesn't affect the calculation of M_T, does affect the calculation of the invariant mass of the two highest p_T tracks, $M(\mu,\mu)$, which is used to remove Z decays from the W data sample:

$$(\cot\theta)_{\text{corrected}} = 1.0004\cot\theta$$

4.4 Absolute Momentum Scale

The final correction to the data sample is to adjust the corrected momentum measured by the CTC to agree with some well measured physical quantity. We choose this quantity to be the world average measurement of the Z mass because

of its high accuracy and the similarity of the transverse momentum distributions of the muons resulting from W and Z decays. The Z mass for Run 1B at CDF has been measured [21] to be 91.110 ± 0.097 GeV. Using the measured world average Z mass value of 91.187 ± 0.007 GeV [4] we find that we need to scale our beam constrained momentum by the factor 1.00085 ± 0.00107.

4.5 The W Recoil Transverse Energy Vector

The neutrino transverse momentum can't be measured directly and so relies on the measurement of the muon momentum, the measurement of the recoil transverse energy vector resulting from the production of the W boson, and the conservation of momentum law. The measured recoil transverse energy vector $\mathbf{u}$ is defined to be the vector sum of the calorimeter transverse energies, relative to the muon vertex, with a correction for the underlying event energy of about 30 MeV per tower in the tower(s) that the muon traversed:

$$\mathbf{u} = \sum_{towers} E^{tower} (\hat{\mathbf{n}} \cdot \hat{\mathbf{r}}) \hat{\mathbf{r}}$$

Here E^{tower} is the energy measured in the electromagnetic or hadronic calorimeter tower, $\hat{\mathbf{n}}$ is the unit vector which points from the event vertex through the center of the tower, $\hat{\mathbf{r}}$ is the radial basis vector in cylindrical coordinates. To calculate $\mathbf{u}$ for the data we use the software package ETFLOW written by Kevin Einsweiler and Young-Kee Kim, using only the tower energies of greater than 5σ above noise level in the calculation.

Note that $\mathbf{u}$ is not a very accurate measurement for two reasons. First, the averaged response $< |\mathbf{u}| >$ normally turns out to be smaller than $< p_T^W >$ since the measured energies of recoiling hadrons are low where calorimeter response is

not linear. Secondly, the underlying event energy correction causes **u** to have a worsened resolution.

4.6 The ν Transverse Momentum Vector

Now that **u** has been defined, we can find the neutrino transverse momentum vector, $\mathbf{p_T^\nu}$, by balancing the momenta of the final state products for the process $p\overline{p} \to WX \to \mu\nu X$ in the transverse plane:

$$\mathbf{p_T^\nu} = -\mathbf{u} - \mathbf{p_T^\mu}$$

4.7 The W Transverse Mass

We then use the definition given in equation 2.5 to calculate the transverse mass of the W boson for every event in our data sample:

$$M_T^2 = (|\mathbf{p_T^\mu}| + |\mathbf{p_T^\nu}|)^2 - (\mathbf{p_T^\mu} + \mathbf{p_T^\nu})^2$$

4.8 W Width Data Sample

The raw data set we begin with is the $W \to \mu\nu$ "MPAD" dataset (MPAD is the PAD dataset with the CTCD bank included) produced by Young-Kee Kim with the selection criteria given in [22]. A summary table of the selection criteria we use to select a data sample with a high concentration of $W \to \mu\nu$ decays is shown in Table 4.1. The reasons for each cut shown are now described. We begin with the 164510 events in the sample that contain one of the second level triggers CMNP_CFT_12_5DEG_V, CMUP_CFT_12_5DEG_V or CMX_CFT_12_5DEG_V. All of these triggers require a CFT (see section 4.1) track match to a track segment in one of the muon detectors. The CMNP_CFT_12_5DEG_V trigger consists of events where a high-p_T muon has traversed the CMU detector only, the

CMUP_CFT_12_5DEG_V trigger consists of events where a high-p_T muon has traversed both the CMU and the CMP detectors, and the CMX_CFT_12_5DEG_V trigger consists of events where a high-p_T muon has traversed the CMX detector only. The CDF "good run" list of October 30, 1996, is then used to filter out those events for which the calorimeters and muon chambers are not all operational. We then check that only one of the second level triggers has triggered for each event. This is to simplify the Monte Carlo simulation where the weight of each trigger needs to be estimated. To improve the likelihood that the candidate CTC track corresponds to a track in one of the muon detectors, several track matching cuts are made in the transverse plane. For the CMNP_CFT_12_5DEG_V trigger, a track matching cut of $|\Delta x_{\rm CMU}| < 2$ cm is imposed, for the CMUP_CFT_12_5DEG_V trigger either $|\Delta x_{\rm CMU}| < 2$ cm or $|\Delta x_{\rm CMP}| < 5$ cm is required, and for the CMX_CFT_12_5DEG_V trigger $|\Delta x_{\rm CMX}| < 5$ cm is required.

We select the highest p_T identified muon to be our candidate muon from a possible W decay. The track parameters found by the CTC for the candidate muon are: p_T^μ, the transverse momentum of the candidate muon derived from the curvature measured by the CTC; z_μ, the z-value measured by the CTC at the point of closest approach of the track to the beam; $\cot\theta_\mu$, the cotangent of the polar angle of track; $\sin\phi_\mu$, the sine of azimuthal angle of the track at its point of closest approach to the beam; and D_0^μ, the impact parameter of the track with respect to the beam. We also identify the highest p_T track (with $p_T > 10$ GeV) that is not the candidate muon, for use in determining if the event should be rejected as being a Z or cosmic ray. It is given the corresponding track parameters $p_T^{\rm track}$, $z_{\rm track}$, $\cot\theta_{\rm track}$, $\sin\phi_{\rm track}$ and $D_0^{\rm track}$. To get a more accurate value of p_T^μ we refit the W candidate muon track to include the VTX determined interaction vertex (of any class) closest to the z_μ value, if within 5 cm of it. Otherwise the W candidate muon track is

refit including the muon track z-value. The x and y coordinates of the vertex are obtained from the SVX$'$ determined beam coordinates. This process is popularly known as "beam constraining" and is done using the TRKSVC subroutine. To determine if the event happens to be a Z, the z_μ and $z_{\rm track}$ are averaged and the VTX vertex closest to the average is looked for. If the found vertex is within 5 cm of both z_μ and $z_{\rm track}$ it is taken to be the event vertex and used to beam constrain the tracks to, otherwise the event vertex is taken to be the average of z_μ and $z_{\rm track}$.

To reduce backgrounds that decrease with increasing p_T, such as $W \to \tau\nu$ decays and heavy flavor and jet production, we make the cuts $p_T^\mu > 25$ GeV/c and $p_T^\nu > 25$ GeV/c. To identify the track as from a muon, we make the minimum ionizing particle cuts $E_{\rm CEM} < 2$ GeV and $E_{\rm CHA} < 6$ GeV. To reduce backgrounds from heavy-flavor decays and jets faking leptons, the recoil transverse energy cut $|\mathbf{u}| < 20$ GeV is imposed.

We require $|z_{\rm vertex}| < 60.0$ cm and $|z_\mu| < 60.0$ cm to keep us within the projective region of the calorimeters and away from the gaps between the central and forward calorimeters. We also require that $|z_{\rm vertex} + 130{\rm cm} \cdot \cot\theta| < 150$ cm to ensure that the tracks traverse every superlayer of the CTC and subsequently have good resolution. To keep only good quality tracks in the sample we require that the number of hits on the stereo layers be at least 12. No cut is made on the number of axial hits because the p_T resolution measurement, which is to be used in the simulation, did not use one.

We remove $Z \to \mu\mu$ events from the sample by identifying events with an opposite sign secondary track with $p_T > 10$ GeV/c which forms an invariant mass $M(\mu^+, \mu^-) > 50$ GeV.

Cosmic ray background could be a significant problem in the 100 GeV $< M_T^W <$ 200 GeV region because there are so few W signal events, and it is not easy to

simulate cosmic rays. The impact parameter cut $|D_0| < 0.15$ cm removes some of these cosmic rays as well as removing events with poorly formed tracks. An effort is made to eliminate any remaining cosmic rays with the following set of specialized cuts.

The following criteria are used to remove cosmic events from the sample: The highest p_T 3D-track other than the W candidate muon ("tight track") with $p_T > 10$ GeV is called the "secondary track".

- Criterion 1: If a hadron calorimeter time $t_{\rm had}$, the time recorded that the track traversed one of the hadron calorimeters, is available for the tight track then we remove events where $|t_{\rm had} - 6.0| > 24.0$ nsec because they are not consistent with the average interaction timing. This criterion removes cosmic rays which arrive at random times outside the normal time window of events originating in the beam.
- Criterion 2: If $t_{\rm had}$ has been measured for both the tight and secondary tracks then events with $\Delta t_{\rm had} = (t_{\rm had})_{\rm top} - (t_{\rm had})_{\rm bot} < -10$ nsec are removed as being consistent with cosmic rays. The subscript "top" refers to tracks with ϕ less than π and "bot" refers to tracks with ϕ greater than π. This criterion removes cosmics which leave tracks that traverse the hadronic calorimeters in the lower region of the detector at least 10 nanoseconds after they traverse hadronic calorimeters in the upper region.
- Criterion 3: Events with both tight and secondary tracks are removed if $|\eta_\mu + \eta_{\rm track}| < 0.2$ and $|\pi - |\phi_\mu - \phi_{\rm track}|| < 0.05$. This criterion removes cosmic events where the constituent tracks are sufficiently close to being back-to-back in η and ϕ.
- Criterion 4: If there is no secondary track but CMU or CMP stub information is available then an event with any stub satisfying $|\pi - |\phi_\mu - \phi_{\rm stub}|| < 0.05$

is removed as being consistent with a cosmic ray. This criterion removes cosmics that do not have a second track in the CTC but do leave a back-to-back stub in the CMU or CMP.

- Criterion 5: Events with both tight and secondary tracks are removed if the 3D angle $\delta\rho = \cos^{-1}(\mathbf{p}_\mu \cdot \mathbf{p}_{\rm track}/p_\mu p_{\rm track}) < 10^\circ$. This criterion identifies cosmics where the timing of the track is so different from that expected, that it causes the track finder software to wrongly reconstruct two tracks close to each other instead of one.

4.9 Summary

As seen in Table 4.1, we have 21824 events in our data sample extracted from the run 1B data taken at CDF. Table 4.2 shows how the events are distributed in the relevant transverse mass regions. The region most important to us is the fit region which determines our statistical uncertainty and contains 196 events. The region we normalize our Monte Carlo transverse mass distribution to, $50 < M_T < 200$ GeV, contains 21791 events.

Table 4.1

Summary of selection criteria used to obtain the W data sample used to find the W width. The number of events passing each cut are shown also.

Selection Criteria	**# pass**
Event passes one of the high p_T muon triggers:	164510
Detector at full operational capacity	157271
$\lvert z_{\rm vertex}\rvert < 60.0$ cm	145795
$\lvert z_{\mu}\rvert < 60.0$ cm	145485
$E_{\rm CEM} < 2$ GeV	110727
$E_{\rm CHA} < 6$ GeV	110070
Track in CTC matches a hit in muon detector	98254
$p_T^{\mu} > 25$ GeV/c	46452
$p_T^{\nu} > 25$ GeV/c	34430
$\lvert\mathbf{u}\rvert < 20$ GeV	31908
Number of hits on stereo layers ≥ 12	26156
$\lvert z_{\mu}(r = 130\text{cm})\rvert < 150.0$ cm	25913
$Z \rightarrow \mu^+\mu^-$ events removed:	23482
Cosmic events are removed	22959
Impact parameter $\lvert D_0\rvert < 0.15$ cm	21824
$0 < M_T < \infty$ GeV	21824

Table 4.2

The number of events in the W data sample in selected transverse mass regions.

Selection Criteria	**# pass**
$0 < M_T < 50$ GeV	15
$50 < M_T < 100$ GeV	21595
$100 < M_T < 200$ GeV (fit region)	196
$200 < M_T < \infty$ GeV	18
$0 < M_T < \infty$ GeV	21824

5. EVENT MODELING

This chapter discusses the generation by Monte Carlo simulation of the theoretical M_T distribution to be used to fit to the W data sample. The simulation consists of two parts, the generation of a $W \to \mu\nu$ event from a $p\overline{p}$ collision and the interaction of the final state particles with the detector. This chapter also discusses the simulation of the background events in the data sample described in Chapter 4.

5.1 Event Generation

This section discusses how $W \to \mu\nu$ events from $\overline{p}p$ collisions can be generated in a Monte Carlo simulation by first generating the events in the $p_T^W = 0$ frame and then boosting the final state particles with an appropriate p_T^W value.

5.1.1 Production and Decay

The W events in the simulation are generated by a zeroth order Monte Carlo event generator called TOYGEN, which sets $p_T^W = 0$ and was developed by the UA2 collaboration. Weighted $\overline{p}p \to W \to \mu\nu(\gamma)(\gamma)$ events* with boson event mass $M = \sqrt{\hat{s}} = \sqrt{x_1 x_2 s}$ and rapidity $y = \frac{1}{2}\ln(x_1/x_2)$ [14] are produced using the differential cross-section distribution

$$\frac{d\sigma}{dx_1 dx_2} \propto \sum_{ij} \frac{F_i(x_1)F_j(x_2)}{x_1 x_2} \cdot |V_{ij}|^2 \cdot \frac{\hat{s}}{(\hat{s} - M_W^2)^2 + (\hat{s},\, {}_W/M_W)^2}$$

*Up to two photons are generated to approximate radiative effects

The functions $F_i(x)$ are provided by the default parton distribution function we use, MRS-R2 [23]. We generate events with $\sqrt{\hat{s}}$ between 30 GeV and 220 GeV to ensure that our simulated events cover the W transverse mass values in our 50 GeV $< M_T^W <$ 200 GeV normalization region sufficiently. The PHOTOS software package [24, 25] is used to generate up to two internal photons to account for the QED radiative effects that may occur in addition to the tree level W decay process.

5.1.2 W Transverse Momentum

The W generally has a non-zero transverse momentum for which the distribution shape needs to be determined for use in the simulation. The p_T distribution of the Z's is simple to measure from dilepton decays. It has been fitted [21] using the following function:

$$\frac{\mathrm{d}N}{\mathrm{d}X} \propto \frac{X^{P_4}}{,\,(P_4+1)}\left[(1-P_1)P_2^{P_4+1}\mathrm{e}^{-P_2X} + P_1P_3^{P_4+1}\mathrm{e}^{-P_3X}\right]; \quad X = p_T/(50.0\ \mathrm{GeV/c})$$

where N is the number of events per bin and P_i are the fit parameters. We use this distribution to generate a p_T value which will be reweighted according to the following prescription, to make it effectively consistent with being from a p_T^W distribution. The p_T distribution function given above does not include the dependence of the p_T^Z distribution on rapidity. The mean absolute rapidity of the data used in the fit is 0.3. We use a weighting function on the events to take into account the rapidity dependence. This function is taken from a theoretical calculation of $\frac{\mathrm{d}\sigma}{\mathrm{d}p_T}(Y=0.3)/\frac{\mathrm{d}^2\sigma}{\mathrm{d}Y\,\mathrm{d}p_T}(Y)$. Finally, we transform to the p_T^W distribution by reweighting each event by the theoretically calculated [26, 27, 28, 29] function $\frac{\mathrm{d}^2\sigma}{\mathrm{d}Y\,\mathrm{d}p_T}(W)/\frac{\mathrm{d}^2\sigma}{\mathrm{d}Y\,\mathrm{d}p_T}(Z)$.

In the simulation, the decay products obtained in section 5.1.1 are then boosted in the transverse plane to give the parent W boson a transverse momentum p_T^W in a randomly chosen direction ϕ.

5.2 Detector Simulation

This section discusses how we simulate the response of the CDF detector to the generated $W \to \mu\nu$ events. The response of the CDF detector can be split into three parts, the muon trigger response, the momentum resolution of the tracking chamber and the recoil transverse energy response and resolution.

5.2.1 Muon Trigger Simulation

All events are initially selected from a list of triggers. The biases and efficiencies of these triggers need to be taken into account in the simulation. The CFT track finding efficiency and its dependence on η_{detector} and ΣE_T [30] are included in the simulation. The muon detector fiducial coverage is also included and combined with the CFT efficiency used to randomly produce stubs in the muon detectors. These stubs are then used to determine which trigger may have seen the event. A special feature of run 1B is the higher luminosity which became high enough sometimes to warrant the blocking of some of the less essential triggers so that only the most important triggers were accepted. This means each trigger has an effective weight relative to the other triggers, referred to as its prescale. The prescales for the CMNP_CFT_12_5DEG_V, CMUP_CFT_12_5DEG_V and CMX_CFT_12_5DEG_V triggers of 0.39, 1.0 and 0.43 respectively [31] were incorporated in the simulation. Each trigger has also had its efficiency at detecting high p_T muons evaluated. Efficiencies of 0.871, 0.861 and 0.696 [32] for the

CMNP_CFT_12_5DEG_V, CMUP_CFT_12_5DEG_V and CMX_CFT_12_5DEG_V triggers respectively are also incorporated in the simulation.

The accuracy of the muon trigger simulation can be examined by considering the simulated muon η and ϕ distributions as compared to the data. Figure 5.1 shows the η and ϕ distribution comparisons are in reasonable agreement, but the data shows an unmodeled asymmetry in the η distribution and a few ϕ sectors where we have overestimated the number of muons in the simulation. These ϕ regions correspond to muon detector towers that were not working properly from time to time during data taking. In section 7.8 we show that the uncertainty in the W width from the trigger simulation is insignificant compared to other systematic errors.

5.2.2 Momentum Resolution

The CTC directly measures curvature ($\propto 1/p_T$) rather than momentum. Thus when we talk about the momentum resolution we are really referring to the resolution of the curvature. The p_T resolution of the CTC after a recalibration by Alan Sill and a realignment by Bill Ashmanskas [20] was found to be $\delta(1/p_T) = \delta p_T/p_T^2 = 0.00091 \pm 0.00004(\mathrm{GeV}/c)^{-1}$ [21]. This resolution has a dependence on the number of hits in the track which in turn depends on the instantaneous luminosity of the event. Thus a correction factor on the resolution is calculated for each event. The resulting corrected resolution is used to smear the p_T of the muon in the simulation. This is done by adding to the unsmeared $1/p_T$ a random number from a Gaussian distribution with mean zero and width corresponding to the corrected resolution.

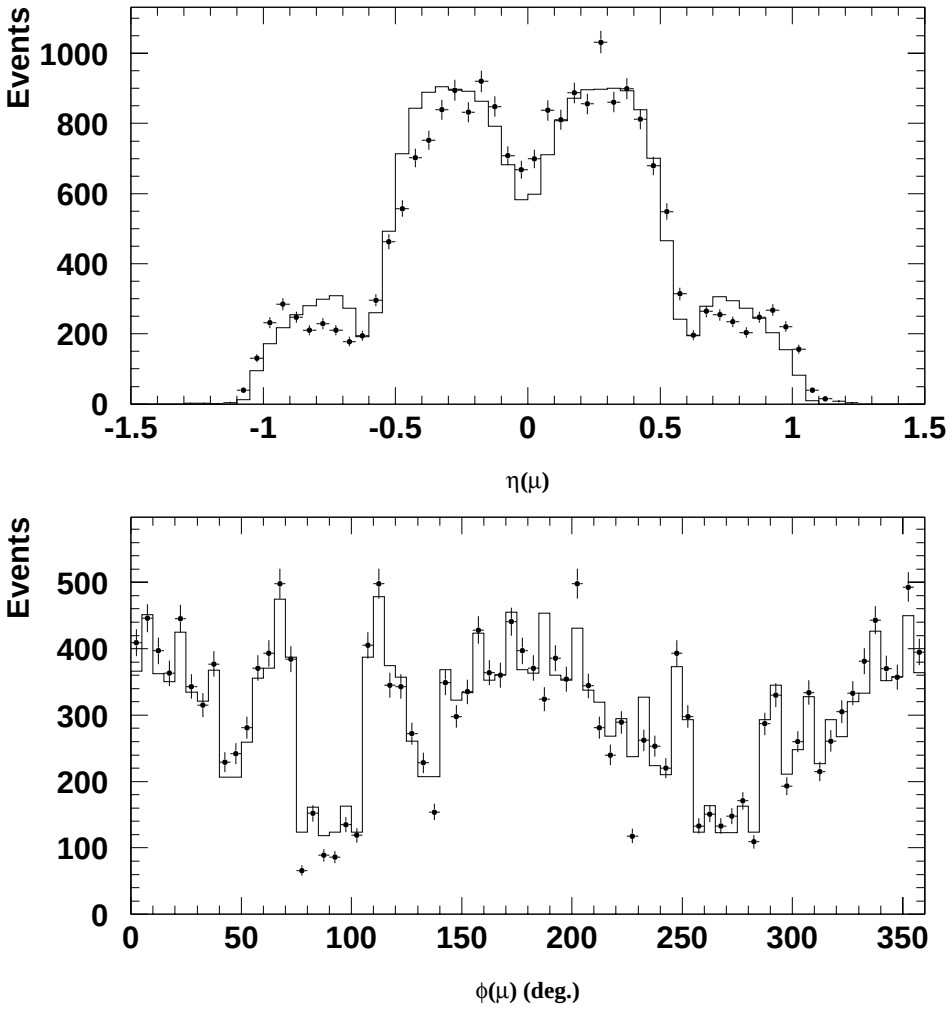

Figure 5.1

Comparison of the Monte Carlo simulation with the muon η and ϕ distributions of the W data sample. The data sample is represented by the points and the simulation is represented by the histogram in both plots.

5.2.3 Recoil Transverse Energy Simulation

The operational definition of the recoil transverse energy vector was described in section 4.5. In the simulation, this measurement needs to be modeled. We need to model both the response and the resolution of the calorimeters to an event with a given W transverse momentum. We define U_1 and U_2 to be the recoil transverse energy vector components in the direction parallel to the direction of the W and the direction rotated by $+\pi/2$ from that direction. The component U_1 for a particular event is then sampled from a Gaussian distribution with mean and standard deviation

$$< U_1 >= P_7 + P_8 p_T^W + P_9 (p_T^W)^2; \quad \sigma(U_1) = \sigma_{\rm MB}(P_{10} + P_{11} p_T^W)$$

where all the P_i values are constants derived from fits to CDF run 1B data. Similarly component U_2 is sampled from a Gaussian distribution with mean and standard deviation

$$< U_2 >= 0; \quad \sigma(U_2) = \sigma_{\rm MB}(P_{12} + P_{13} p_T^W)$$

In the above equations, $\sigma_{\rm MB}$ is the minimum bias resolution function and is given by

$$\sigma_{\rm MB} = P_5 (\Sigma E_T)^{P_6}$$

where P_5 and P_6 are taken from fits to minimum bias data. The scalar sum of all transverse energy in the calorimeters has the distribution

$$\Sigma E_T \propto Q_2, \, (Q_1 + 1)$$

where Q_1 and Q_2 are obtained from fits to the Z boson ΣE_T distribution, and are dependent on p_T^Z:

$$Q_1 = P_1 + P_2 p_T^Z; \quad Q_2 = P_3 + P_4 p_T^Z$$

A correction to this calculated recoil transverse energy vector needs to be made to include the effect of any internal photons emitted during the W production. Internal photons can have two effects on the detector simulation. If the photon strikes the same tower as the muon, its energy is measured by the calorimeter in addition to the energy deposited by the muon. This can cause the event to be rejected if the photon(s) cause $E_{\rm CEM}$ to go above the cut energy of 2 GeV. This case is simulated by extracting a random energy deposited by the muon from the data $E_{\rm CEM}$ distribution and then adding to it the photon(s) energy, where we have assumed all the photon energy has been deposited in the CEM. The event is then rejected if $E_{\rm CEM} > 2$ GeV. If the photon strikes a different tower to that the muon traverses, then it will be measured as part of the recoil transverse energy vector. This is allowed for in the simulation by adding the photon(s) transverse momentum vector to the recoil transverse energy vector previously calculated.

The resulting recoil transverse energy distributions $|\mathbf{u}|$, $u_{||}$ and $u_{\perp}$ (generated at the world average value $, _W = 2.1$ GeV) are then compared to the data in figures 5.2, 5.3 and 5.4. The χ^2 values per number of degrees of freedom for each of these fits are 1.6, 1.5 and 1.8 respectively. For our purposes, the most important quantity to fit correctly is $u_{||}$, which, as indicated by Equation 2.8, is the dominant recoil transverse energy component of the W transverse mass. The simulated $u_{||}$ distribution, the histogram plot shown in figure 5.3, agrees very well with the mean and standard deviation of the data. There is also a good agreement between the data and the simulation in both the peak and tail regions.

5.3 Backgrounds

There are processes other than the $W \rightarrow \mu\nu$ process that can get into the W width data sample, despite the cuts used to minimize them. These background

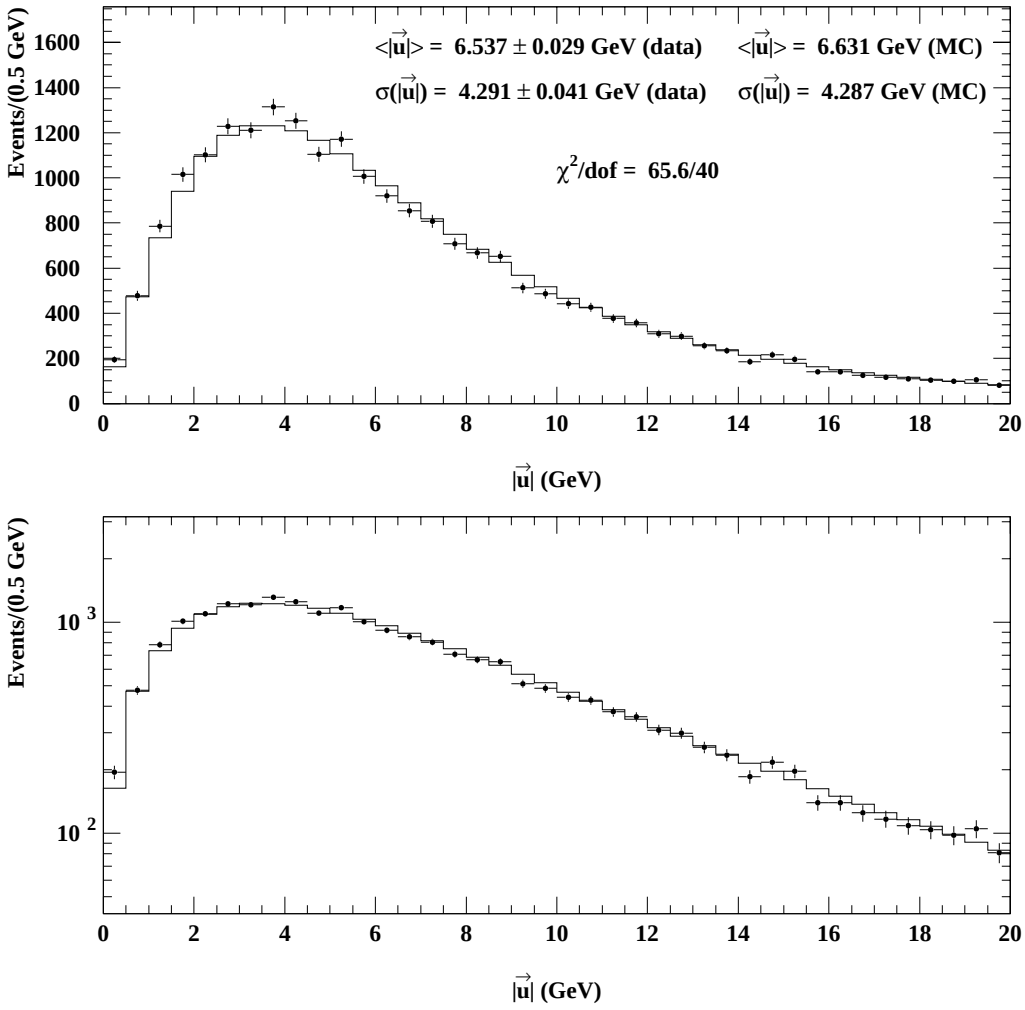

Figure 5.2

Comparison between the $W \to \mu\nu$ data and Monte Carlo (MC) simulations of the $|\vec{\mathbf{u}}|$ distribution, for , $_W = 2.1$ GeV.

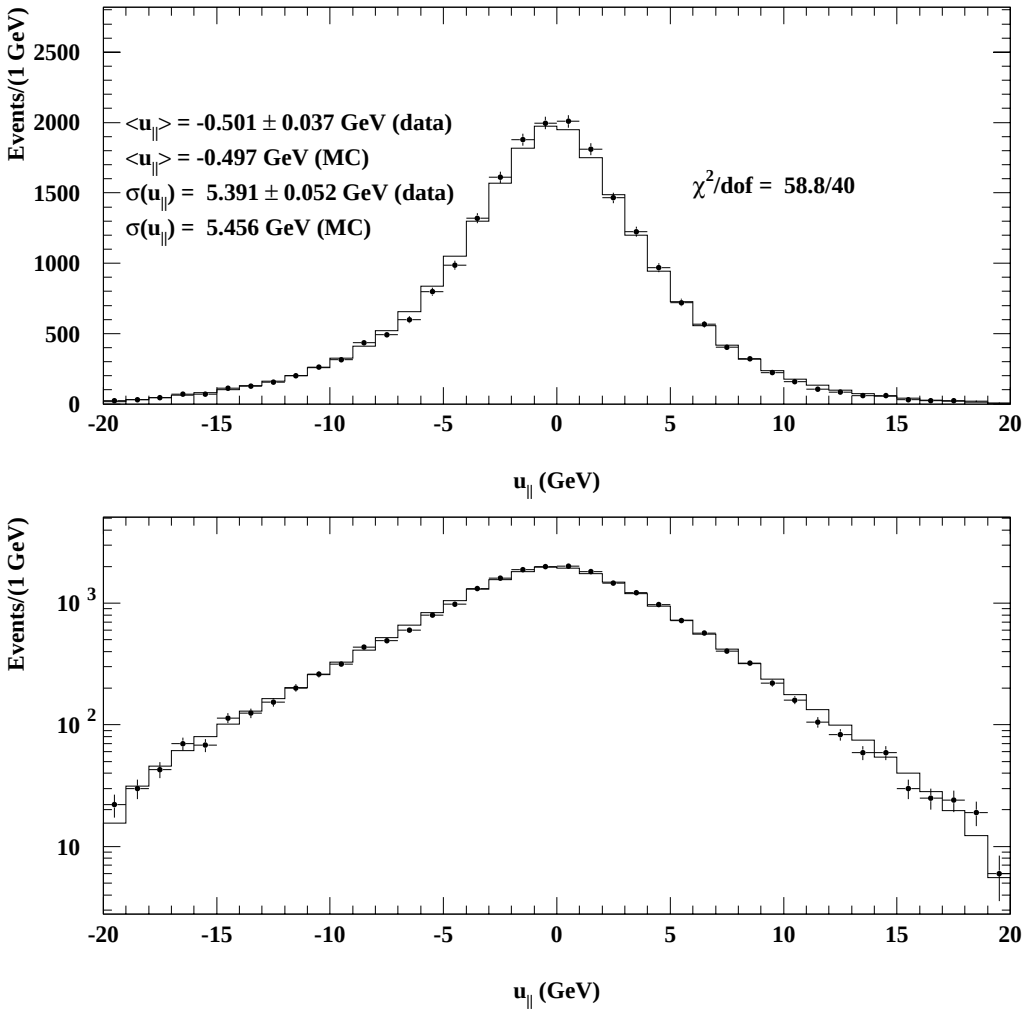

Figure 5.3

Comparison between the $W \to \mu\nu$ data and Monte Carlo (MC) simulations of the $u_{\parallel}$ distribution, for , $_W = 2.1$ GeV.

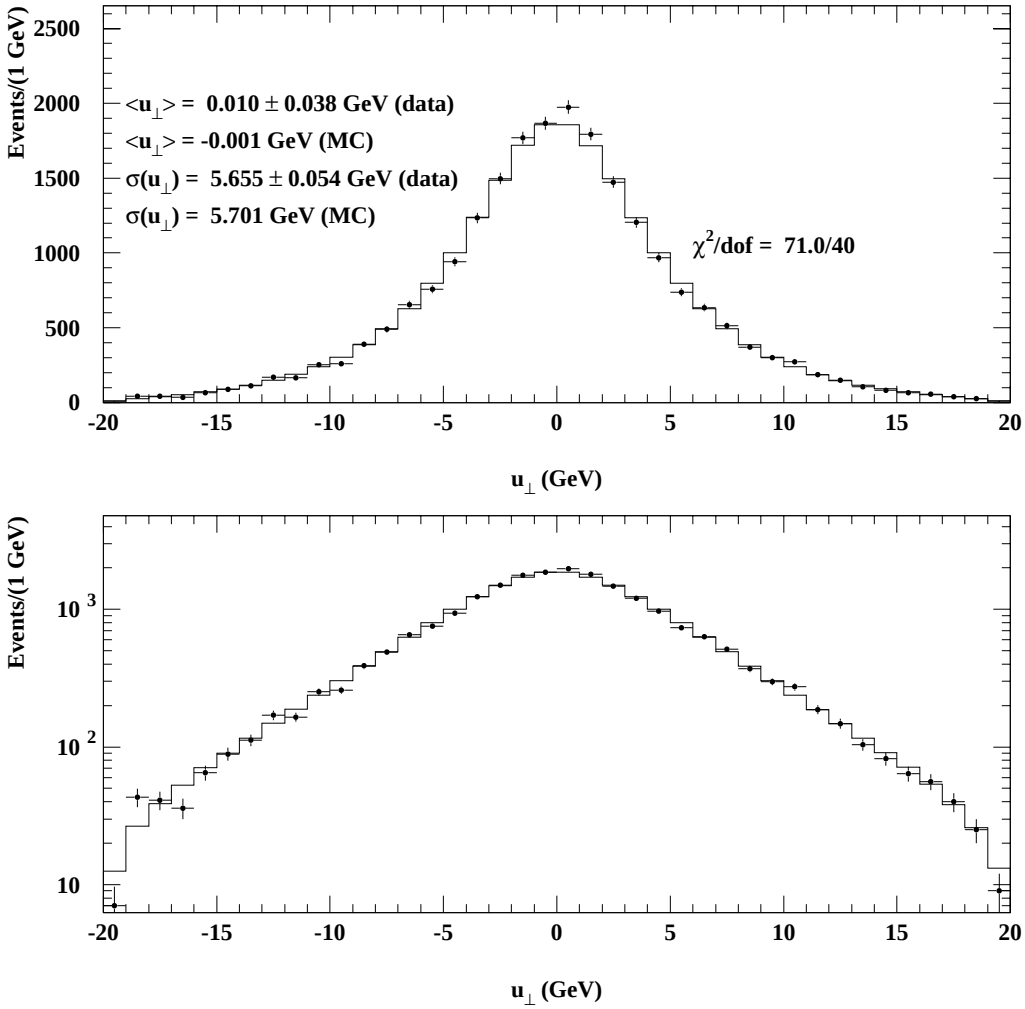

Figure 5.4

Comparison between $W \to \mu\nu$ data and Monte Carlo (MC) simulations of the $u_\perp$ distribution, for , $_W = 2.1$ GeV.

processes generally have different M_T distributions from that of the $W \to \mu\nu$ process and consequently can result in an error in the W width if not properly simulated. This section contains a description of how we estimate the M_T distributions of each background.

5.3.1 $Z \to \mu\mu$

The $Z \to \mu(\mu)$ background mainly comes from $Z \to \mu\mu$ events where one of the tracks is not detected by the CTC. This is usually because the track traverses the CTC either partially or not at all, causing it to be in the class of tracks where the track finding efficiency is less than one. To simulate this background, the TOYGEN generator is used to produce $Z \to \mu\mu$ decays. An algorithm uses the trigger efficiencies and the detector geometry to determine which of the muons would have been identified as the W muon. The recoil model is the same as that used for the $W \to \mu\nu$ signal but with a correction for the fact that the muon with the missing track will still deposit a typical muon energy in the calorimeters. The corrected recoil transverse energy vector is given by $\mathbf{u}_{\text{corrected}} = \mathbf{u} + E_{CAL}\mathbf{p}^{\mu}/|\mathbf{p}^{\mu}|$ where deposited energy $E_{CAL} = E_{CEM} + E_{CHA}$ is obtained from the muon tracks in the $W \to \mu\nu$ data sample. The W data sample selection cuts are then applied and the remaining events are given a weighting based on the probability that the track of the second muon is not found by the CTC and the event therefore not rejected as a consequence of the $Z \to \mu\mu$ event removal criteria as given in section 4.8.

When the $Z \to \mu(\mu)$ background is included in the Monte Carlo simulation, a level of 761 ± 28 events (3.5% of the data) in the $50 < M_T < 200$ GeV region and 5 ± 2 events (2.6% of the data) in the $100 < M_T < 200$ GeV region are estimated. The M_T distribution of the generated $Z \to \mu(\mu)$ background can be seen in figure 5.9

5.3.2 $W \to \tau\nu$

The $W \to \tau\nu \to \mu\nu\nu\nu$ background is virtually indistinguishable from the $W \to \mu\nu$ signal because the three neutrinos together mimic the single neutrino of our signal. The TOYGEN generator is used to produce W's which are then decayed into $\tau\nu$ and then the τ is decayed into $\mu\nu\nu$. The simulation then follows the W transverse lineshape model as explained in sections 5.1 and 5.2. The background level contributed by this type of event is found to be 2.1% compared to the $W \to \mu\nu$ signal in the 50 GeV $< M_T <$ 200 GeV normalization region and 0.9% for the 100 GeV $< M_T <$ 200 GeV fit region. Assuming a fit for the W width has been obtained without the $W \to \tau\nu \to \mu\nu\nu\nu$ background, inclusion of this background in the Monte Carlo simulation causes the normalization factor applied to the 50 GeV $< M_T <$ 200 GeV region to drop by about 2.1%, but this would cause the simulation level to drop further than 0.9% predicted background level in the 100 GeV $< M_T <$ 200 GeV region, making the simulation curve lower than the data. Refitting would need to take place which would require that the width increase to match the simulation to the data again. Thus we expect the addition of this background to give a positive shift in , $_W$.

This background yields 438 ± 21 events over the normalization region and $2 \pm \sqrt{2}$ events in the fit region, when included in the Monte Carlo simulation. The M_T distribution of the generated $W \to \tau\nu \to \mu\nu\nu\nu$ background can be seen in figure 5.9.

5.3.3 Heavy-Flavor Decays and Fakes (QCD)

A significant fraction of proton-antiproton collisions cause di-jet processes where two jets are produced back to back. Jet processes are described by the theory of Quantum Chromodynamics, which is commonly abbreviated as QCD.

These di-jet events can mimic $W \rightarrow \mu\nu$ processes in two main ways. A heavy flavor quark in one of the jets can decay into particles that include a high-p_T muon (eg. $b \rightarrow c\mu\nu$). In this type of decay, the b needs to have a high p_T to give the decay offspring muon and neutrino enough p_T to pass the selection criteria of the W data sample. This leads to the decay products $c\mu\nu$ having relatively small opening angles with each other and consequently the muon and neutrino are parallel to one of the jets. The second kind of di-jet event that mimics a W event, is one where a constituent hadron is misidentified as a muon. In this case, the energy in one of the jets needs to have been mismeasured enough to give the appearance that a high missing-E_T particle is present. To summarize we expect that the missing E_T and muon will have azimuthal directions close to the directions of the jets. A measure of this effect is the azimuthal angle that the missing E_T makes with the highest E_T jet, $\phi_{\nu,\text{jet}}$ and the azimuthal angle that the muon direction makes with the highest E_T jet, $\phi_{\mu,\text{jet}}$. In both of the background processes mentioned, the muon, being located inside a jet, will have at least a few tracks near to it. A measure of the extent of the muon isolation is the quantity ΣP_T, the sum of the track scalar P_T values greater than 1.0 GeV/c within a cone of size $\Delta R = \sqrt{(\Delta\phi)^2 + (\Delta\eta)^2} = 0.4$ about the muon (the sum excludes the primary muon track).

We can split the W data sample in the transverse mass region $50 < M_T < 200$ GeV into a non-isolated muon sample with $\Sigma P_T > 2$ GeV/c and an isolated muon sample with $\Sigma P_T < 2$ GeV/c. The $\phi_{\nu,\text{jet}}$ and $\phi_{\mu,\text{jet}}$ distributions for the non-isolated muon and isolated muon samples are shown in figure 5.5. From the non-isolated muon distributions we see a significant increase in the number of events in the regions $150^\circ < \phi_{\nu,\text{jet}} < 180^\circ$ and $0^\circ < \phi_{\mu,\text{jet}} < 30^\circ$, which are presumably due to the presence of QCD background.

Assuming that the non-isolated events in the region $30^\circ < \phi_{\nu,\text{jet}} < 150^\circ$ are predominantly real W events, we can estimate the number of real non-isolated W events in the regions $0^\circ < \phi_{\nu,\text{jet}} < 30^\circ$ and $150^\circ < \phi_{\nu,\text{jet}} < 180^\circ$ by assuming that the real non-isolated W events have the same ϕ distribution as the isolated ones. Subtracting out this number from the total number of events observed in those regions yields the estimate of 171.0 QCD events in $50 < M_T < 200$ GeV region and 107.9 QCD events in $65 < M_T < 200$ GeV region for fake neutrinos that are close to a jet. An alternative method is to fit a line through the distribution over $30^\circ < \phi_{\nu,\text{jet}} < 150^\circ$ and extend it into the remaining regions, finding the excess of the data over the fitted line. In the $50 < M_T < 200$ GeV and $65 < M_T < 200$ GeV regions, 166.1 QCD events and 109.3 events are found respectively. Repeating the above analysis for the $\phi_{\mu,\text{jet}}$ distribution using the shape normalization method yields 181.6 and 114.8 QCD background events in the $50 < M_T < 200$ GeV and $65 < M_T < 200$ GeV regions respectively. Using the linear fit method we obtain 180.8 and 126.8 events in the $50 < M_T < 200$ GeV and $65 < M_T < 200$ GeV regions respectively.

Averaging all of the above measurements yields 175 ± 13 QCD background events in $50 < M_T < 200$ GeV region and 115 ± 11 QCD background events in $65 < M_T < 200$ GeV region.

To find the shape of the M_T distribution for the QCD background we define a data sample that has a high concentration of QCD events. We require that the neutrino satisfies $0^\circ < \phi_{\nu,\text{jet}} < 15^\circ$ or $165^\circ < \phi_{\nu,\text{jet}} < 180^\circ$, and that the muon satisfies $0^\circ < \phi_{\mu,\text{jet}} < 15^\circ$ or $165^\circ < \phi_{\mu,\text{jet}} < 180^\circ$. Figure 5.6 shows the M_T distributions for decreasing levels of isolation of the muon.

In the $70 < M_T < 100$ GeV region, the M_T distributions take an approximately exponential shape for less isolated muons. Doing an exponential fit in the

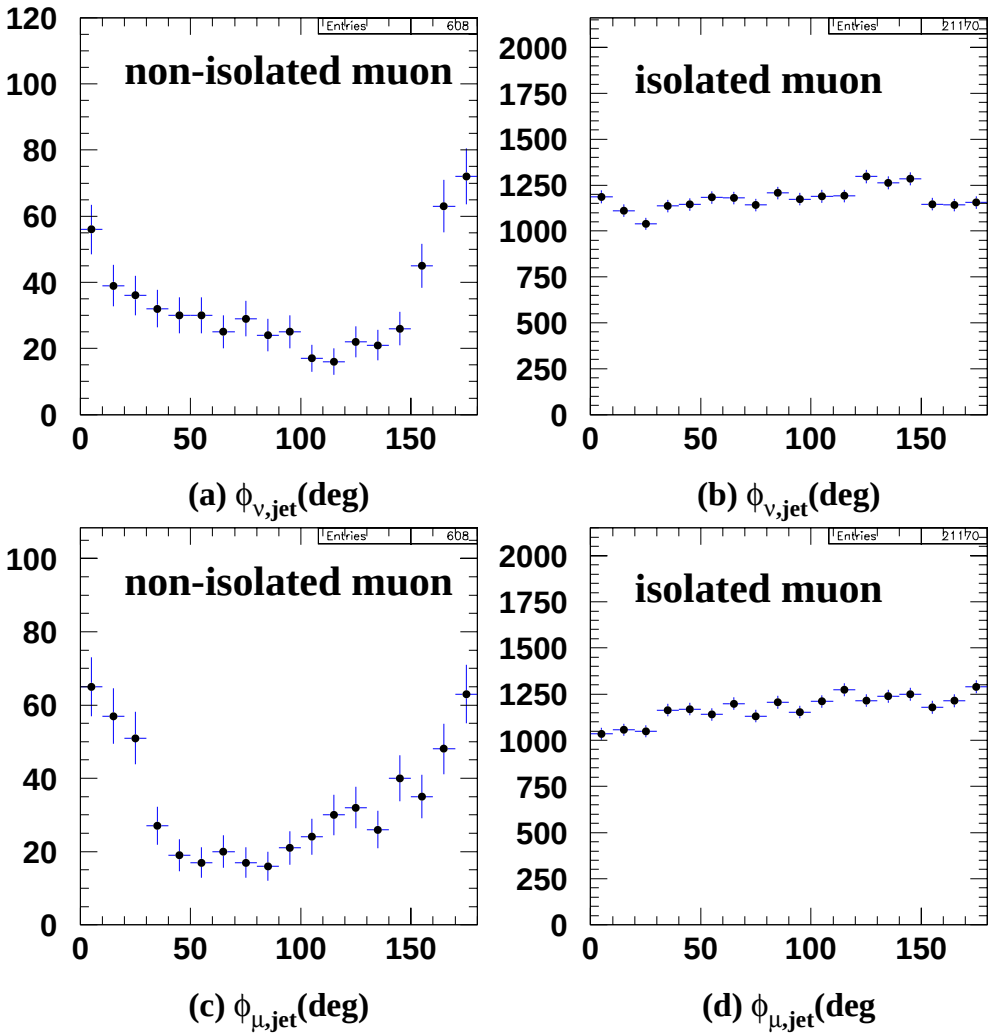

Figure 5.5

Plots (a) and (b) are distributions of the angle between the missing-E_T direction and the direction of the highest E_T jet for non-isolated muons and isolated muons. Plots (c) and (d) are distributions of the angle between the muon direction and the direction of the highest E_T jet for non-isolated muons and isolated muons. The transverse mass region used is $50 < M_T < 200$ GeV.

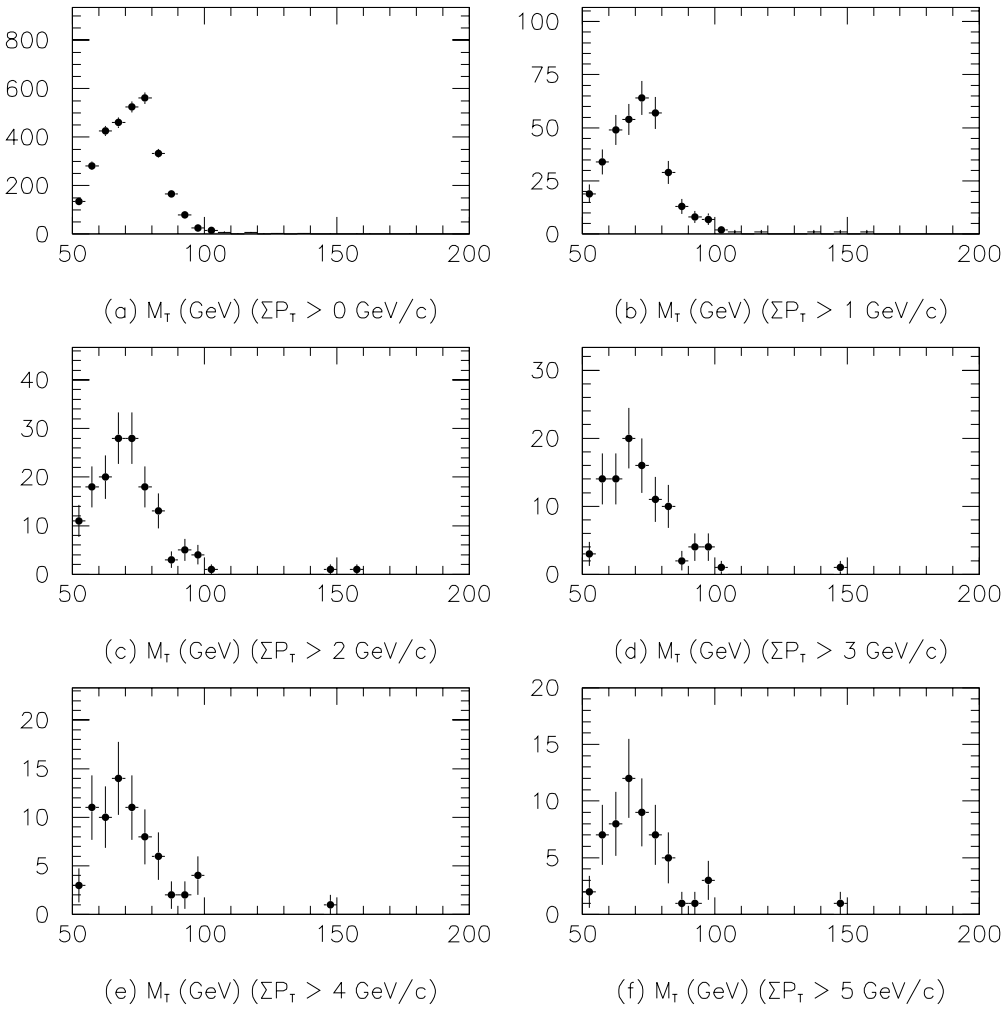

Figure 5.6

M_T distributions for various levels of isolation of the muon. The data sample used is the W data sample with the additional requirement that the neutrino satisfies $0^\circ < \phi_{\nu,\mathrm{jet}} < 15^\circ$ or $165^\circ < \phi_{\nu,\mathrm{jet}} < 180^\circ$, and that the muon satisfies $0^\circ < \phi_{\mu,\mathrm{jet}} < 15^\circ$ or $165^\circ < \phi_{\mu,\mathrm{jet}} < 180^\circ$.

$70 < M_T < 100$ GeV region of the $\Sigma P_T > 3$ GeV/c plot yields the smallest uncertainty in the decay constant. The $\Sigma P_T > 3$ GeV/c plot contains 100 events in the $50 < M_T < 200$ GeV region and 69 events in $65 < M_T < 200$ region which is in agreement with the ratio of the previously predicted numbers of 175 and 115 QCD events in those regions, within their uncertainties. This plot will be used to obtain the functional form of the QCD background M_T distribution. A Gaussian function is used to fit the region $50 < M_T < 70$ GeV and an exponential function is used to represent the remaining data. An exponential is fit to the data in the $70 < M_T < 100$ GeV region while being constrained to give the observed number of data events in the region $100 < M_T < 200$ GeV. This is to ensure that the representative function gives the correct number of events in the monte carlo fit region used to obtain the W width. The complete fit to the 100 events of the highly non-isolated muon data is shown in figure 5.7.

Scaling the fitted function to the 175 QCD events we predict for our entire sample, we estimate 4 ± 2 QCD background events in the $100 < M_T < 200$ GeV region. The M_T distribution of the QCD background can be seen in figure 5.9.

5.3.4 Cosmic Rays

It is possible to individually visually scan the signal events in the $100 < M_T < 200$ GeV/c^2 region of the W data sample to find out how many cosmic rays are left in the sample since there are only 196 events. There were found to be no cosmics in a scan. We would also like to be able to find the number of cosmic rays in the $50 < M_T < 100$ GeV/c^2 region since the simulation is normalized over this region. Scanning the 21584 events in this region would take a very long time so instead we look at the much smaller set of events (outside of the W data sample) which have an impact parameter magnitude $|D_0|$ greater than 0.15 cm

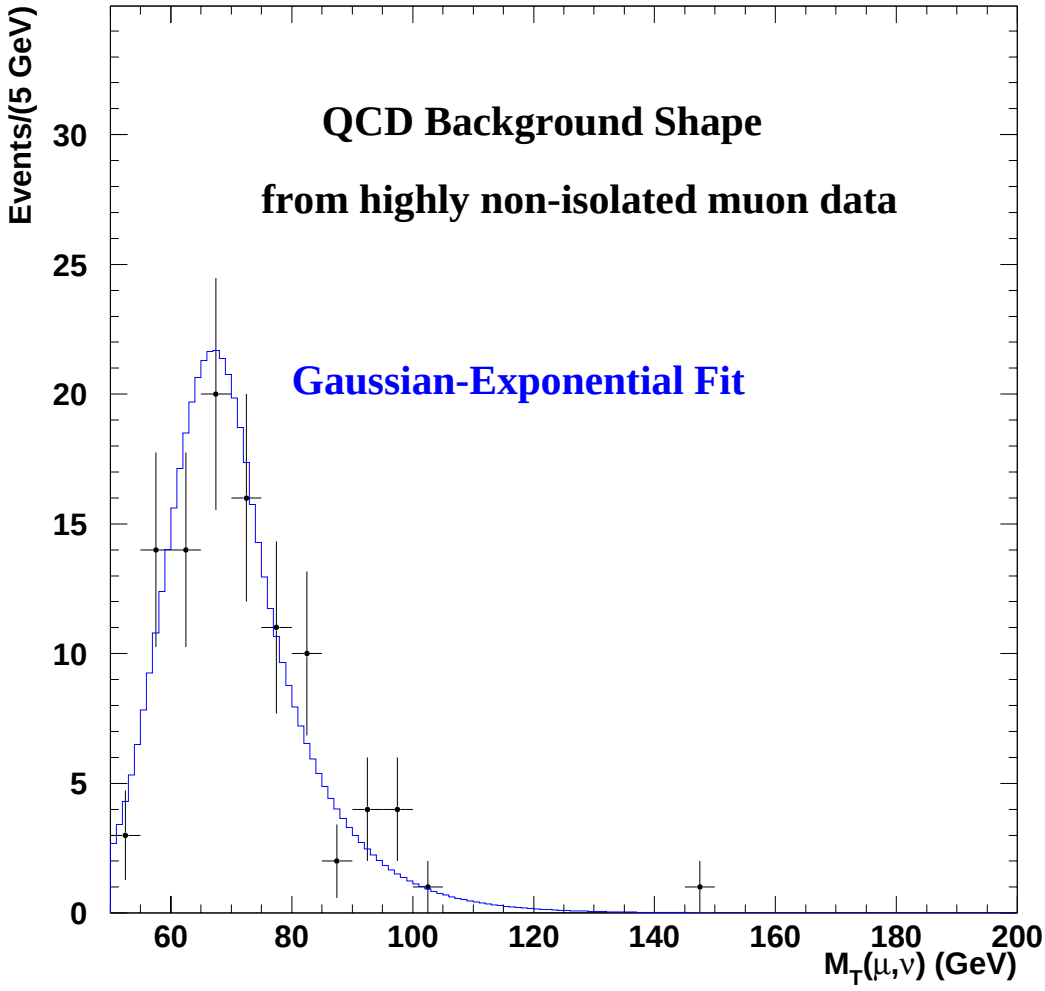

Figure 5.7

Combined Gaussian and exponential fit to a highly non-isolated muon data sample made by requiring that $\Sigma P_T > 3$ GeV/c, and that the neutrino satisfies $0^\circ < \phi_{\nu,\text{jet}} < 15^\circ$ or $165^\circ < \phi_{\nu,\text{jet}} < 180^\circ$, and that the muon satisfies $0^\circ < \phi_{\mu,\text{jet}} < 15^\circ$ or $165^\circ < \phi_{\mu,\text{jet}} < 180^\circ$. This shape is used as the QCD background shape in the Monte Carlo simulations.

in the $50 < M_T < 100$ GeV/c^2 region but pass all the other W data sample selection criteria. This high impact parameter data sample should have a higher concentration of cosmics than the W data sample and thus we can use its impact parameter distribution to extrapolate back into the $|D_0| < 0.15$ cm region to approximate the number of cosmics located there. This sample contains 838 events in the 0.15 cm $< |D_0| <$ 0.80 cm region, of which 16 are positively identified as cosmic events. The remaining 822 events are assumed to have poorly reconstructed tracks. The distributions of $|D_0|$ and M_T are plotted in figure 5.8. The $|D_0|$ distribution of the identified cosmics (shown as the darker histogram) appears flat. A flat fit to the impact parameter distribution yields 4 ± 2 ($\{0.018 \pm 0.009\}\%$) cosmic events predicted for the cosmic ray background in the $50 < M_T < 100$ GeV/c^2 region. The cosmic ray background is modeled as a linear transverse mass distribution in the $50 < M_T < 100$ GeV/c^2 region where the slope is obtained from the high impact parameter data sample. The shape of the transverse mass distribution for the cosmic ray background is shown in figure 5.9.

5.3.5 Summary of simulated backgrounds

The transverse mass lineshapes of the backgrounds and the total background shape are compared in Figure 5.9.

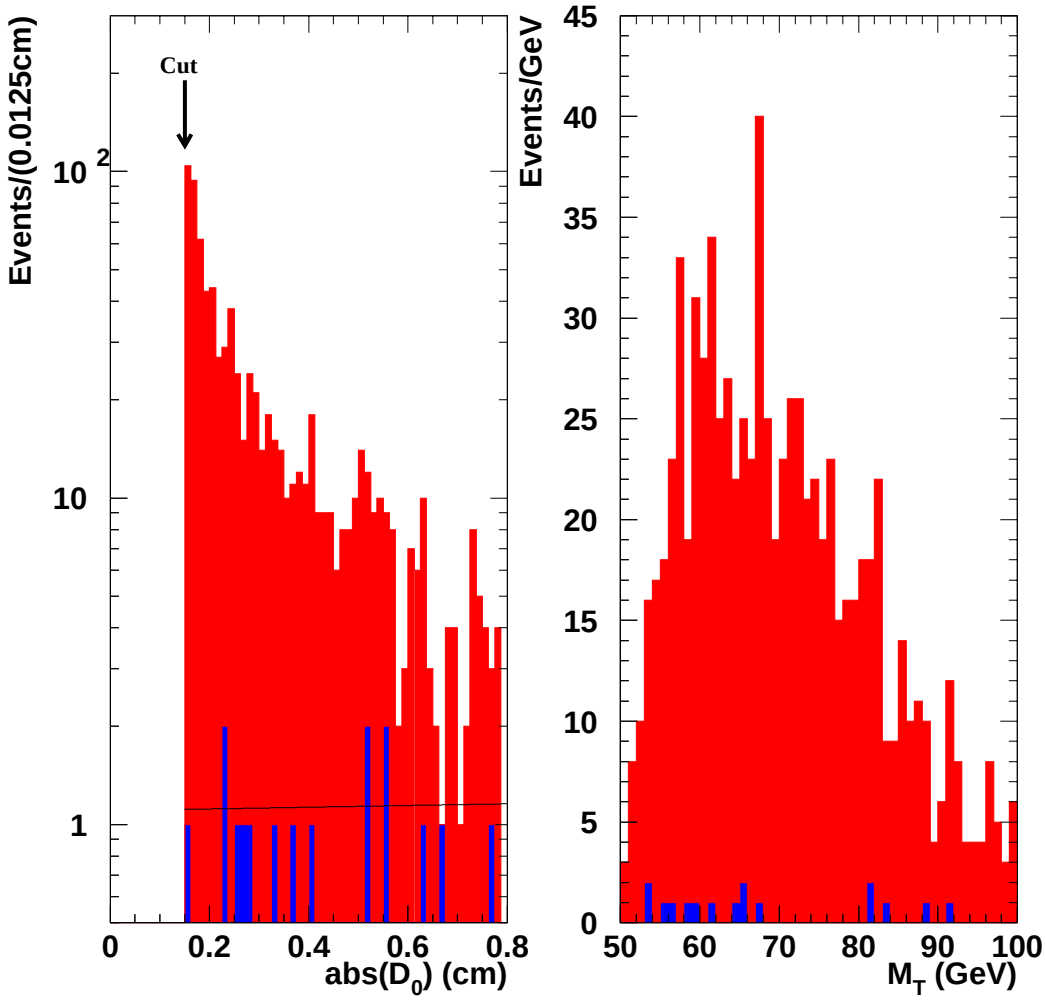

Figure 5.8

Distributions of $|D_0|$ and M_T for events with 0.15 cm $< |D_0| <$ 0.8 cm that pass the W selection criteria. Darker shaded histograms indicate identified cosmic rays.

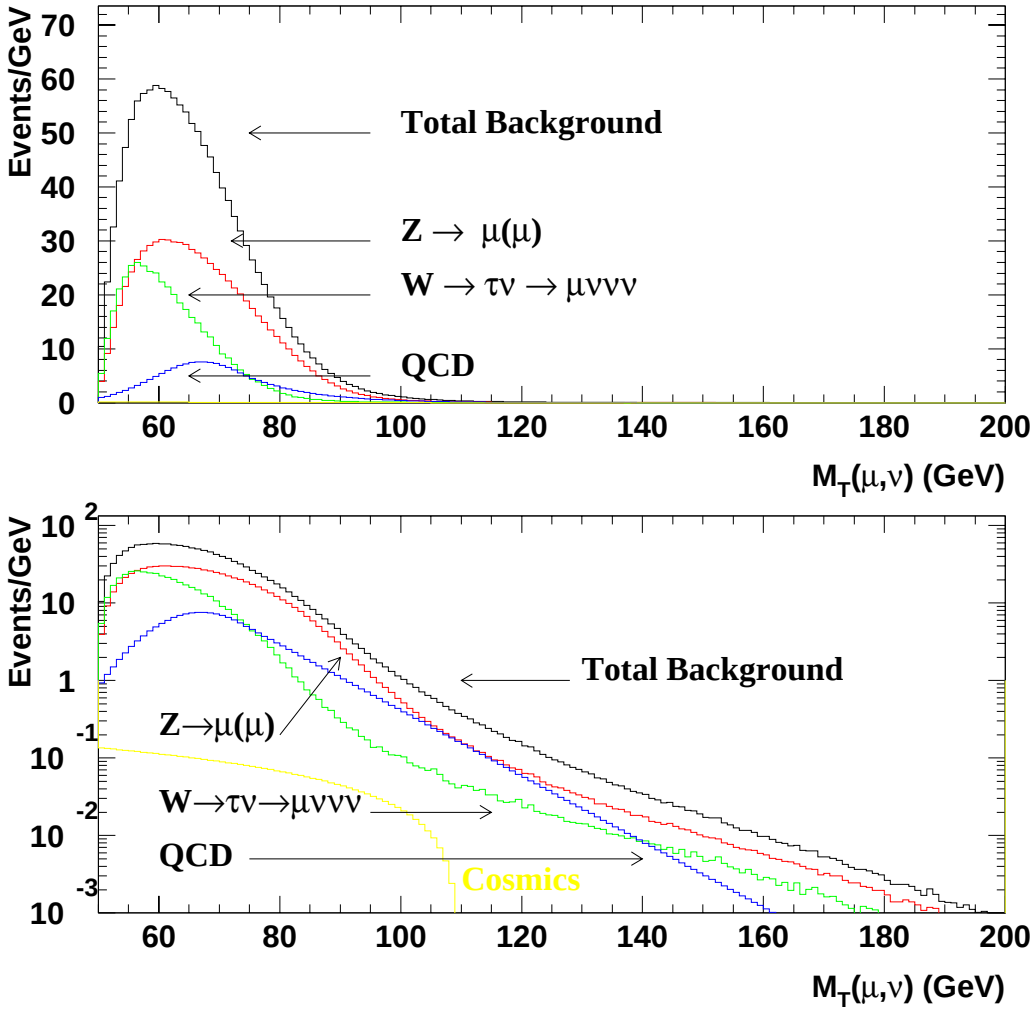

Figure 5.9

Predicted M_T distribution of all backgrounds and total background.

6. W WIDTH FIT

6.1 Fitting Method

The W width is obtained by finding the value of , (W) which provides the closest fitting Monte Carlo M_T distribution to the W data sample M_T distribution. A measure of the closeness of this fit is a quantity called the "likelihood" which is defined by

$$L = \prod_i \frac{\mu_i^{x_i} \mathrm{e}^{-\mu_i}}{x_i!}$$

which is the product of the Poisson probabilities that the simulated number of events in each bin is equal to the number of data events observed. The quantity x_i is the number of observed events in the i-th transverse mass bin and μ_i is the Monte Carlo expected number of events in that bin. To obtain the best fit we need to maximize the likelihood. A simplification to this method is to take the natural logarithm of the likelihood, whereby if, as it usually is, the likelihood plot versus width is close to a Gaussian shape, then the $\ln(L)$ will be close to being quadratic shaped, which is easier to fit. Further, minimum turning points are generally easier to fit than maximum turning points, and so the $-\ln(L)$ function is the most convenient to use. Computationally it is:

$$-\ln(L) = \sum_i [\mu_i - x_i \cdot \ln(\mu_i) - \ln(x_i!)]$$

To find the uncertainty in the fit quantity it is noted that in general, the range of , values corresponding to values of $-\ln(L)$ greater than the minimum value by the amount 0.5 have a 68% probability of containing the true value of , . This

is an analogy to the one standard deviation probability of the fit value within a perfect Gaussian distribution. This method enables us to determine even possibly asymmetrical statistical uncertainties.

6.2 Width Determination and Statistical Uncertainty

In section 2.2 we noted that the transverse mass distribution is sensitive to the W width especially over the range 100 GeV $< M_T <$ 200 GeV. We choose this region to fit our Monte Carlo simulation to the W data sample. Because of the low statistics (196 events) in this region it is impractical to normalize the number of events in the Monte Carlo simulation in this region. We can confidently simulate the $W \to \mu\nu$ and background processes over the range 50 GeV $< M_T <$ 200 GeV where we have almost all of the W data sample, so we use the 21791 events in that range to normalize to.

Using the results of the Monte Carlo simulations we have done, we make templates of the M_T distribution for the $W \to \mu\nu$ signal and the $Z \to \mu(\mu)$, $W \to \tau\nu \to \mu\nu\nu\nu$, QCD and cosmic backgrounds for the span of values $\Gamma_W = 1.0, 1.1, \ldots, 3.0$. For each Γ_W we add the signal and background M_T distribution templates together into one overall template representing the Monte Carlo M_T distribution. We then calculate the $-\ln(L)$ value of the comparison of this Monte Carlo simulation M_T distribution with our data M_T distribution. We find that we can accurately fit the $-\ln(L)$ values versus Γ_W with a cubic polynomial. The minimum of this curve yields a measured Γ_W value of 1.791 GeV. On a $-\ln(L)$ curve, a standard deviation in the statistical accuracy of the parameter being plotted against corresponds to the shift in that parameter that causes an increase in the $-\ln(L)$ value by 0.5 above its minimum value. Applying this analysis to the width range $1.0 < \Gamma < 3.0$ GeV yields that, including statistical uncertainty, Γ_W is $1.791^{+0.193}_{-0.184}$ GeV.

This uncertainty level means that we are fitting $-\ln(L)$ out to at least 6 standard deviations in , . We may be biasing our fit by including such a wide range of , values away from the best fit value. To improve the accuracy of the fit, we choose the smaller fit range $1.4 <$, $_W < 2.2$ GeV as shown in figure 6.1, which makes the fit region just over 2 standard deviations from the minimum of $-\log(L)$. This yields the value of , $_W = 1.779^{+0.198}_{-0.187}$ GeV, which we take to be our W width and statistical uncertainty. As a check on this value we choose fit regions up to 3 standard deviations wide and after refitting find that , $_W$ changes by less than 1 MeV.

Figure 6.2 shows the transverse mass distributions of the W data sample, the Monte Carlo simulation (including background), and the total background template generated for , $_W = 1.779$ GeV. The χ^2 values per number of degrees of freedom for this fit over the $50 < M_T < 200$ GeV and $100 < M_T < 200$ GeV regions are 72.6/71 and 26.2/23 respectively. These χ^2 values have probabilities of 42% and 29% respectively.

6.3 Check on Statistical Uncertainty

As a check on the statistical uncertainty we evaluated in section 6.2 we make a set of 100 simulated Monte Carlo data samples of the same size as our observed data sample, generated at our fit value of , $_W = 1.779$ GeV. We then fit our Monte Carlo simulation of 50 million events to each of these fake data samples and obtain the statistical uncertainty for each. The distributions of the positive and negative statistical uncertainties are shown in figure 6.3. Our measured values of the positive and negative statistical uncertainties of -187 MeV and 198 MeV agree well with the mean values shown in the plots. Also shown are the fitted , values which have a mean of 1.753 ± 0.017 GeV which shows that the simulation has a

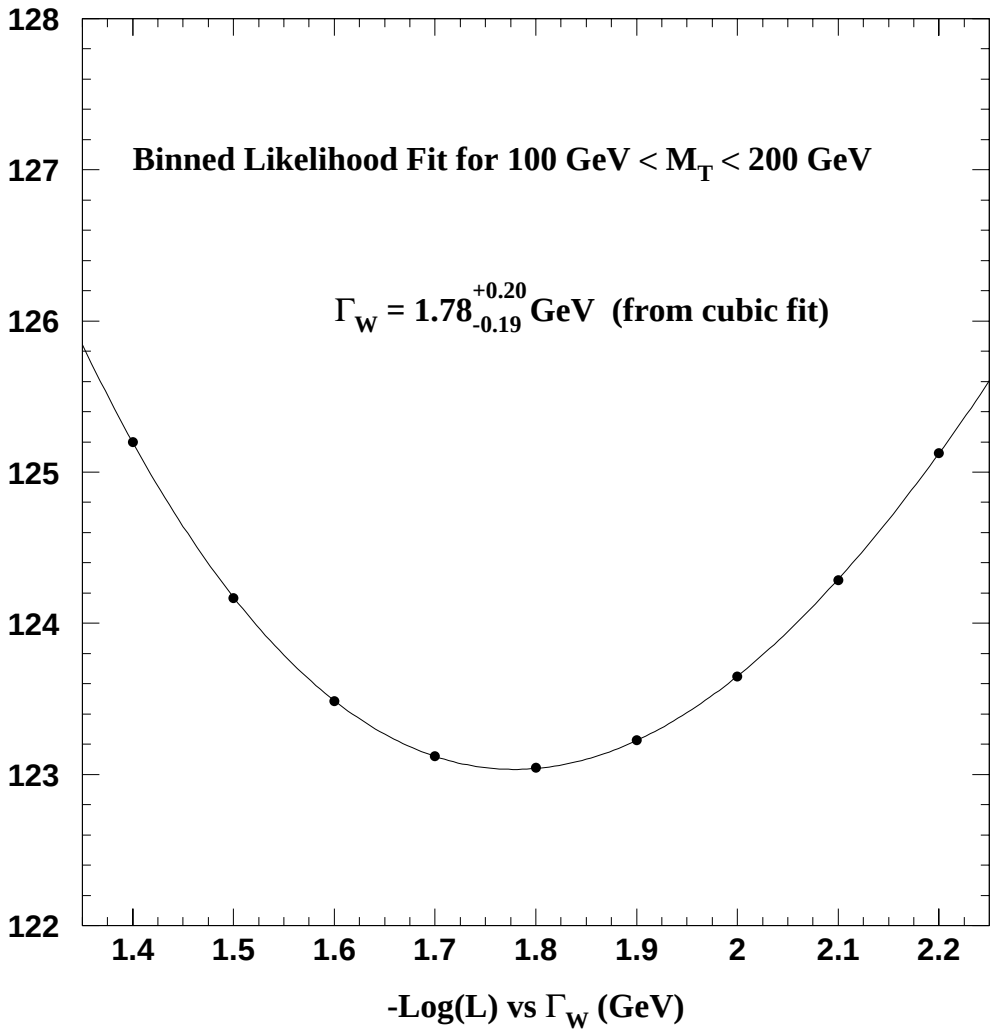

Figure 6.1

Plot of negative log of the likelihood function calculated from the Monte Carlo simulation comparison to the W data sample transverse mass distribution over the range 100 GeV $< M_T <$ 200 GeV, for various simulation input values of , $_W$. The simulation is normalized to the W data sample over the range 50 GeV $< M_T <$ 200 GeV. The shown W width fit value is calculated from the location of the minimum value of $-\ln(L)$ in a third-order polynomial fit.

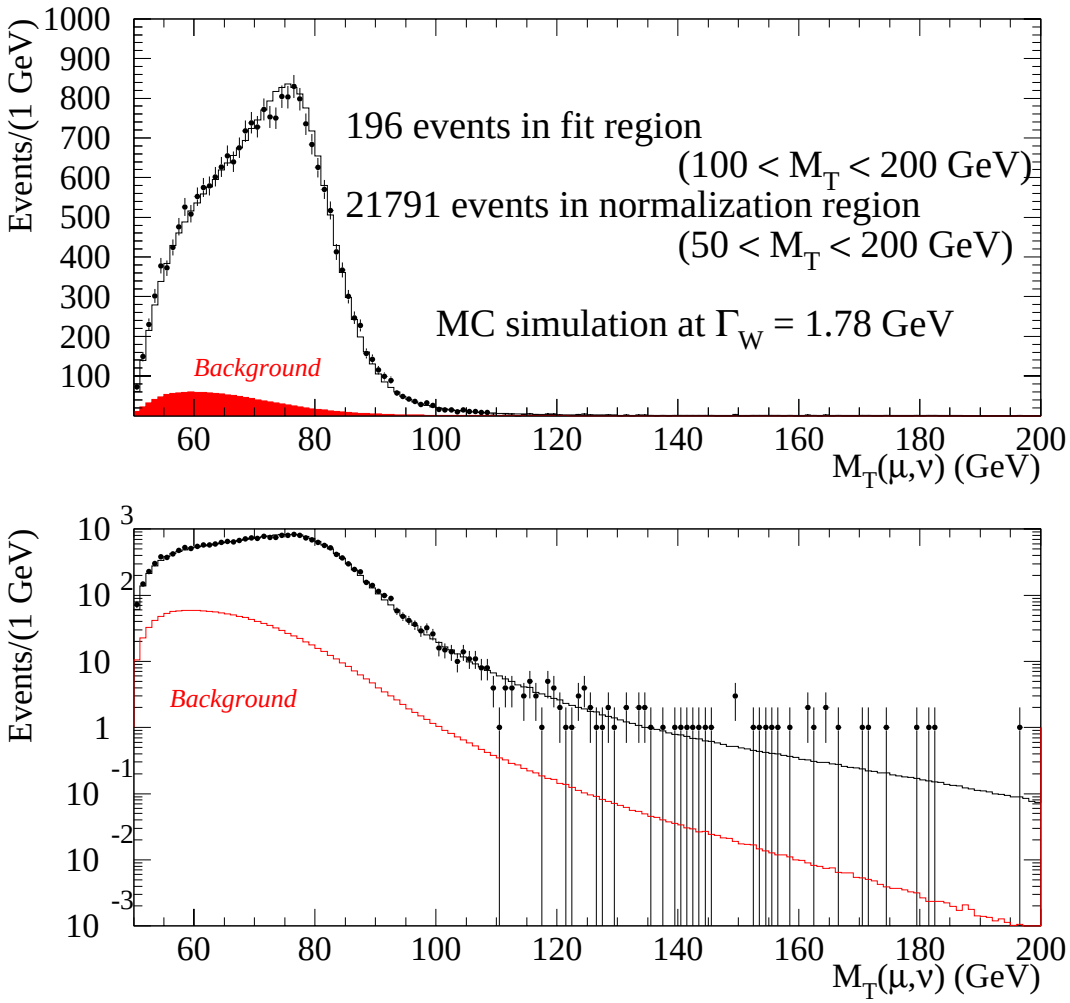

Figure 6.2

M_T distributions of W data sample, Monte Carlo simulation and total background.

small bias of -26 ± 17 MeV. The final plot shown is the distribution of the number of events in the fit region predicted by our Monte Carlo. The 196 events in our data sample easily lie within a standard deviation of the mean value of 203 events shown.

6.4 High W Transverse Mass Region

In the high transverse mass region, $M_T > 200$ GeV, we observe 18 events, of which 2 are visually identified as cosmic events which eluded our cuts, leaving 16 ± 4 non-cosmic events. Using our Monte Carlo simulation to generate 50 million events in the region $90 < \sqrt{\hat{s}} < 1800$ GeV with $, _W = 1.779$ GeV, we produce the M_T distribution shown in Figure 6.4. The distribution has been normalized to the 185 $W \to \mu\nu$ events we estimate to be in the data in the $100 < M_T < 200$ GeV region. The distribution then predicts 8 $W \to \mu\nu$ events in the region $M_T > 200$ GeV. Not including backgrounds in the simulation, we therefore have an agreement of the Monte Carlo simulation with the data to within 2 standard deviations of the number of data events in the $M_T > 200$ GeV region. Including the backgrounds would make the agreement better.

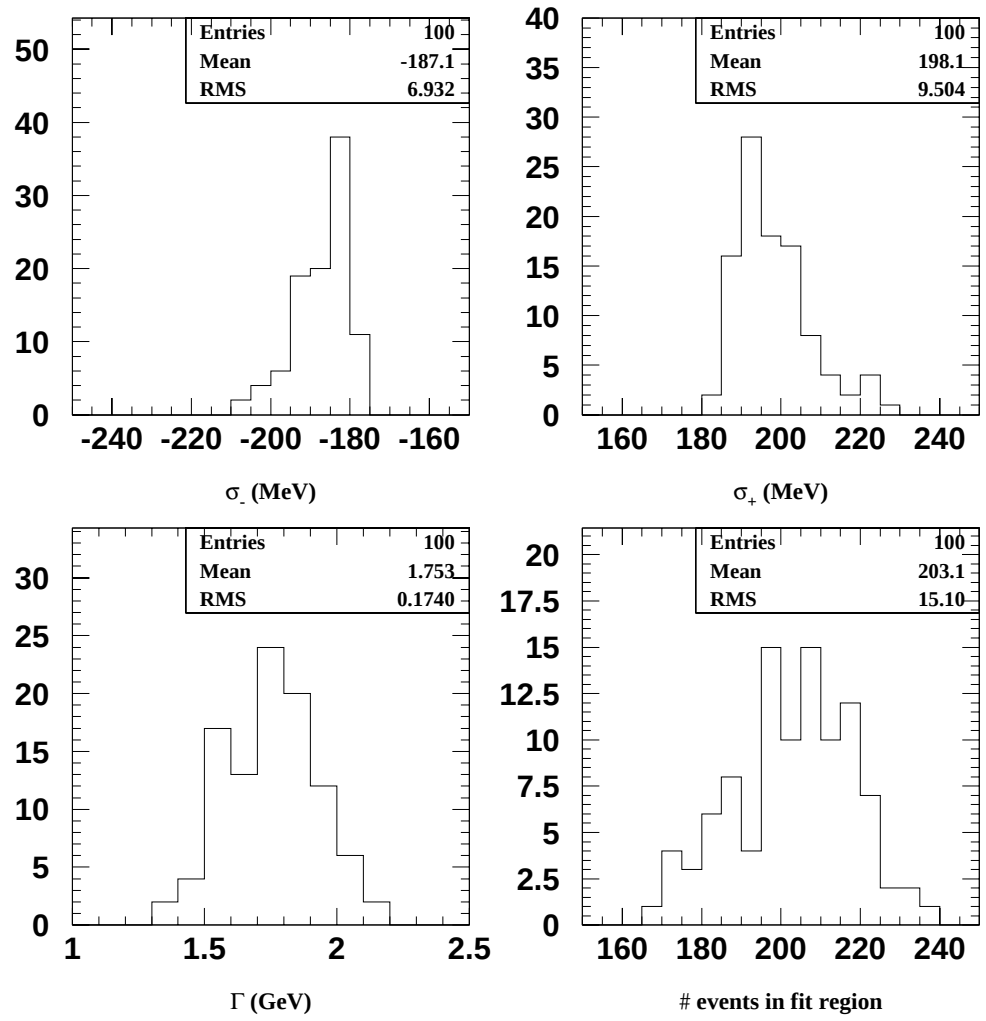

Figure 6.3

Distributions of σ_- and σ_+, the negative and positive uncertainties in the W width, the fitted values of the W width, and the number of fit region events for a sample of 100 transverse mass distributions with the same number of events as our data sample, generated at , $_W = 1.779$ GeV by the Monte Carlo simulation.

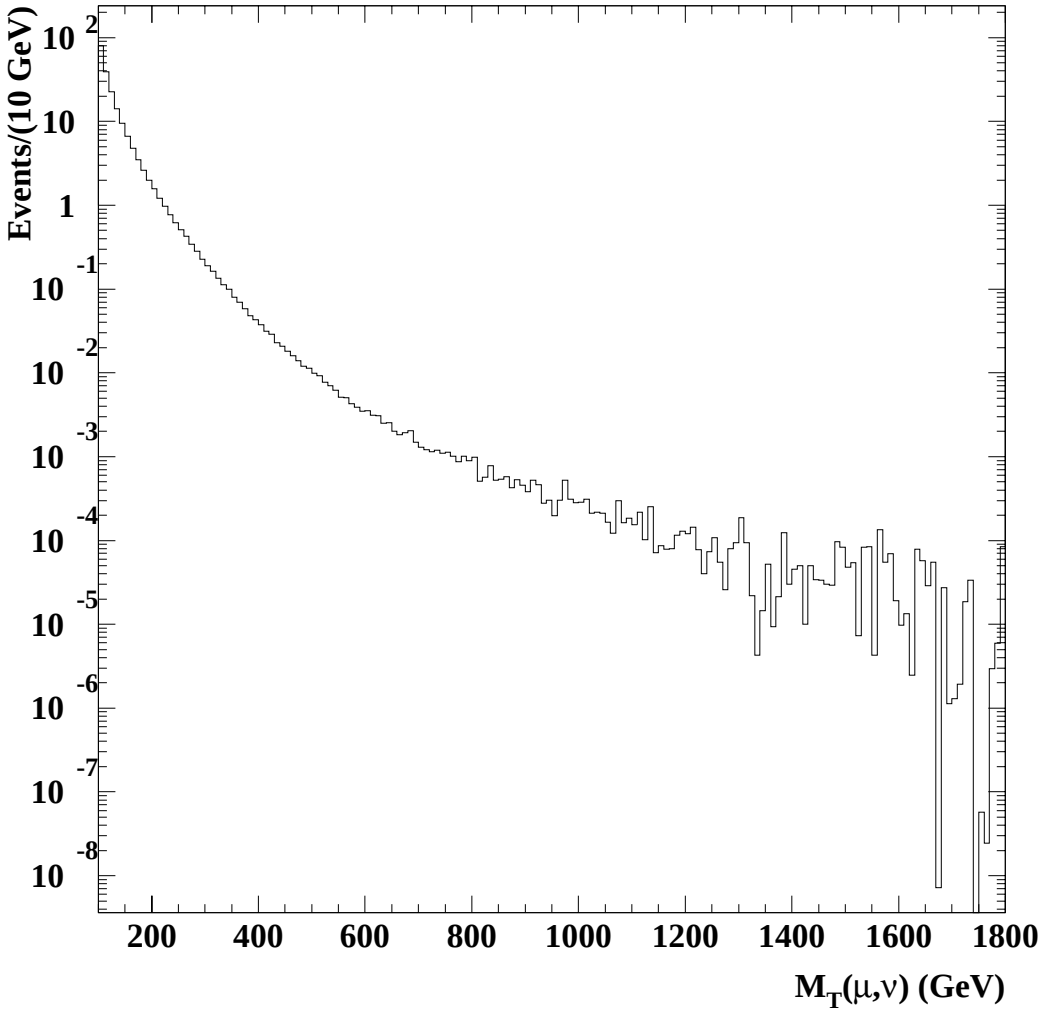

Figure 6.4

M_T distribution of $W \to \mu\nu$ Monte Carlo simulation over the $100 < M_T < 1800$ GeV region.

7. W WIDTH SYSTEMATIC UNCERTAINTIES

This chapter describes the determination of the systematic uncertainties in the measured W width.

7.1 Fitting Method

The ideal Monte Carlo simulation would generate an infinite number of events. Since we are limited by practical constraints to a finite number of events, there will be some variation in the Γ_W fit value dependent on the set of random numbers we choose. This effect is sometimes called "fitter jitter". Our reported Γ_W fit value is derived from a simulation containing 50 million generated events. Splitting our 50 million simulated events into 10 subsets of 5 million events, and extracting W width values for each subset, we find that the uncertainty in the mean width is 5 MeV, which is what we take to be our fit method uncertainty.

7.2 Muon Momentum Scale

As described in section 4.4, we apply a scale factor of 1.00085 ± 0.00107 to the beam constrained transverse momentum of the candidate muons. We fluctuate this scale factor with Gaussian statistics 50 times and apply each sampled scale factor to our unscaled data sample, creating 50 separate scaled data samples. Fitting a 50 million event Monte Carlo simulation to each of these scaled data samples yields the distribution of Γ_W deviations from the central fit value shown in figure 7.1. A

Gaussian fit to this distribution has a standard deviation of 15 ± 2 MeV. Therefore we estimate the uncertainty in , $_W$ from the muon momentum scale to be 15 MeV.

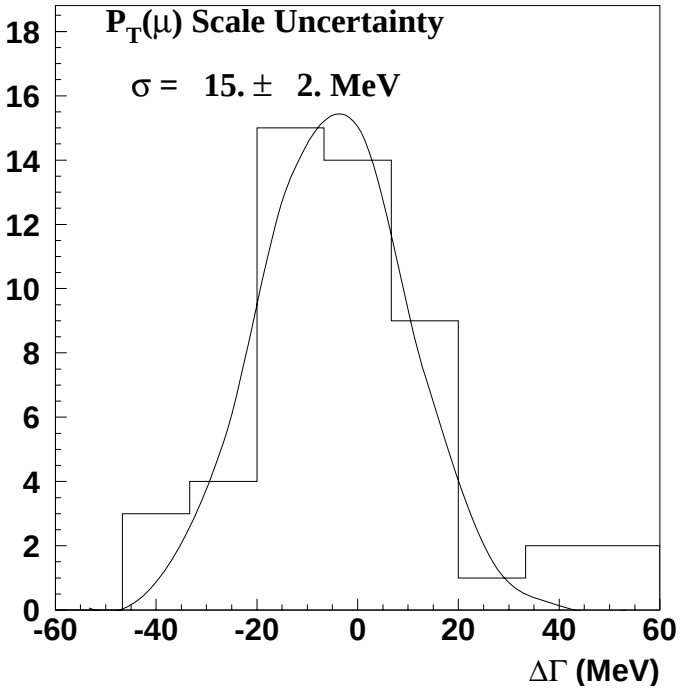

Figure 7.1

The variation in , (W) from the variation of the p_T^μ scale.

7.3 Muon Momentum Resolution

The p_T resolution of the CTC was found from Run 1B studies of $Z \to \mu\mu$ decays [21] to be $\delta p_T/p_T^2 = 0.000912 \pm 0.000040(\mathrm{GeV}/c)^{-1}$. We sample the p_T resolution with Gaussian statistics 20 times, and create Monte Carlo simulations for each value. Fitting those simulations to our data sample, we find a standard deviation

of 18 MeV in , (W), and use this as our uncertainty due to the p_T resolution uncertainty.

7.4 *W* Transverse Momentum

The p_T distribution for the W bosons in the event generator part of the Monte Carlo simulation is determined in the same manner as for the W mass measurement from muons [21]. The least accurate component of this calculation is the representation of the $Z \to \mu\mu$ data p_T^Z distribution with the following 4 parameter function:

$$\frac{\mathrm{d}N}{\mathrm{d}X} \propto \frac{X^{P_4}}{,\ (P_4+1)} \left[(1-P_1)P_2^{P_4+1}\mathrm{e}^{-P_2 X} + P_1 P_3^{P_4+1}\mathrm{e}^{-P_3 X}\right]; \quad X = p_T/(50.0\mathrm{GeV/c})$$

where

$$P_1 = 0.51356 \quad P_2 = 0.27675 \quad P_3 = 7.81930 \quad P_4 = 0.41704$$

The correlated uncertainties in these parameters are given by the covariance matrix

$$V = \begin{pmatrix} 0.23943 & 0.22097 & 0.040949 & 0.045029 \\ 0.22097 & 0.20485 & 0.037930 & 0.041612 \\ 0.040949 & 0.037930 & 0.0072297 & 0.0078078 \\ 0.045029 & 0.041612 & 0.0078078 & 0.0095174 \end{pmatrix}$$

which can be used to generate random parameter sets, by the "square root method" [33], for use in determining the uncertainty in , $_W$.

The "square root method" involves extracting the lower-triangular matrix C from V by using the following recursive formulae:

$$\begin{aligned} C_{i1} &= V_{i1}/\sqrt{V_{11}} && 1 \le i \le m \\ C_{ii} &= \left|V_{ii} - \textstyle\sum_{k=1}^{i-1} C_{ik}^2\right|^{1/2} && 1 < i \le m \\ C_{ij} &= \frac{V_{ij} - \sum_{k=1}^{i-1} C_{ik}C_{jk}}{jj} && 1 < j < i \le m \end{aligned}$$

and then finding the randomly distributed parameter set P_i' from

$$P_i' = \sum_j C_{ij} R_j + P_i$$

where R_j is a vector of random numbers extracted from a Gaussian distribution with zero mean and unit variance.

From a sample of 144 such parameter sets and 1.5 million simulated events, we obtain the distribution of W width shifts as shown in figure 7.2. A Gaussian fit to this distribution has a standard deviation of 69 ± 5 MeV. Therefore we estimate the uncertainty in , $_W$ from the input $p_T(W)$ distribution to be 69 MeV.

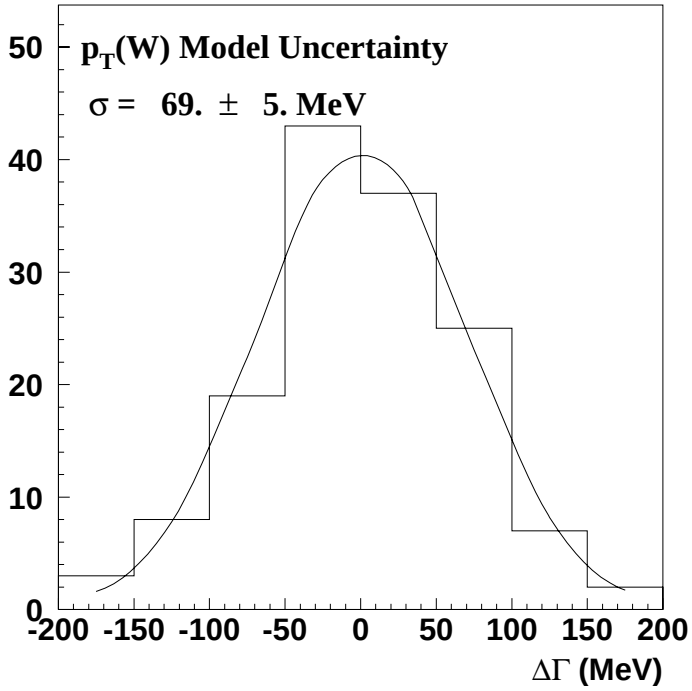

Figure 7.2

The variation in , (W) from a sample of $p_T(W)$ distributions.

7.5 Recoil Transverse Energy Model

The recoil transverse energy model was described in section 5.2.3. The fit parameters, as derived from $W \to \mu\nu$ and minimum bias data at CDF in run 1B, are listed below.

$$P_1 = 1.2852, \quad P_2 = 0.099309, \quad P_3 = 22.421, \quad P_4 = -0.21066,$$
$$P_5 = 0.324, \quad P_6 = 0.577, \quad P_7, = -0.50798, \quad P_8 = -0.57666,$$
$$P_9 = -0.00051, \quad P_{10} = 0.94174, \quad P_{11} = 0.01860, \quad P_{12} = 0.90071,$$
$$P_{13} = -0.00556$$

The parameters P_7 - P_{13} have significantly larger uncertainties than P_1 - P_6 and the correlations between their uncertainties are represented by the following covariance matrix:

$$V = \begin{pmatrix} 0.4315 \times 10^{-1} & -0.6439 \times 10^{-2} & 0.1671 \times 10^{-3} & 0.3664 \times 10^{-3} \\ -0.6439 \times 10^{-2} & 0.1333 \times 10^{-2} & -0.3922 \times 10^{-4} & -0.7773 \times 10^{-4} \\ 0.1671 \times 10^{-3} & -0.3922 \times 10^{-4} & 0.1343 \times 10^{-5} & 0.2441 \times 10^{-5} \\ 0.3664 \times 10^{-3} & -0.7773 \times 10^{-4} & 0.2441 \times 10^{-5} & 0.1373 \times 10^{-2} \\ -0.3859 \times 10^{-4} & 0.8219 \times 10^{-5} & -0.2574 \times 10^{-6} & -0.9293 \times 10^{-4} \\ 0.1775 \times 10^{-11} & -0.2928 \times 10^{-12} & 0.8476 \times 10^{-14} & 0.2158 \times 10^{-12} \\ -0.1248 \times 10^{-12} & 0.1750 \times 10^{-13} & -0.5025 \times 10^{-15} & -0.5989 \times 10^{-14} \end{pmatrix}$$

$$\begin{pmatrix} -0.3859 \times 10^{-4} & 0.1775 \times 10^{-11} & -0.1248 \times 10^{-12} \\ 0.8219 \times 10^{-5} & -0.2928 \times 10^{-12} & 0.1750 \times 10^{-13} \\ -0.2574 \times 10^{-6} & 0.8476 \times 10^{-14} & -0.5025 \times 10^{-15} \\ -0.9293 \times 10^{-4} & 0.2158 \times 10^{-12} & -0.5989 \times 10^{-14} \\ 0.1115 \times 10^{-4} & -0.1609 \times 10^{-13} & 0.6114 \times 10^{-15} \\ -0.1609 \times 10^{-13} & 0.1388 \times 10^{-2} & -0.8657 \times 10^{-4} \\ 0.6114 \times 10^{-15} & -0.8657 \times 10^{-4} & 0.8821 \times 10^{-5} \end{pmatrix}$$

We use the above covariance matrix and the "square root method", as described in section 7.4, to produce Gaussian distributed random parameter sets representing variations in the recoil transverse energy model, with the correlations between the parameters taken into account.

From a sample of 150 such parameter sets applied to the standard binary sample of 50 million generated events, the resulting , (W) distribution (see figure 7.3) is found to be Gaussian and has a width of 87 MeV.

7.6 Parton Distribution Functions

The parton distribution functions or PDF's are used in the Monte Carlo simulation to determine the rapidity dependence of the generated W bosons. A number of different PDF's have been devised that fit the $|\eta| < 1$ charge asymmetry data [21] : MRS-R1, MRS-R1(MOD), MRS-R2, MRS-R2(MOD), MRS-T, and MRS-T(MOD). The qualifier MOD refers to the fact that the PDF has been modified from the original version to a form that expresses an agreement with the CDF asymmetry data. The fit that each PDF makes with the asymmetry data is shown in figure 7.4.

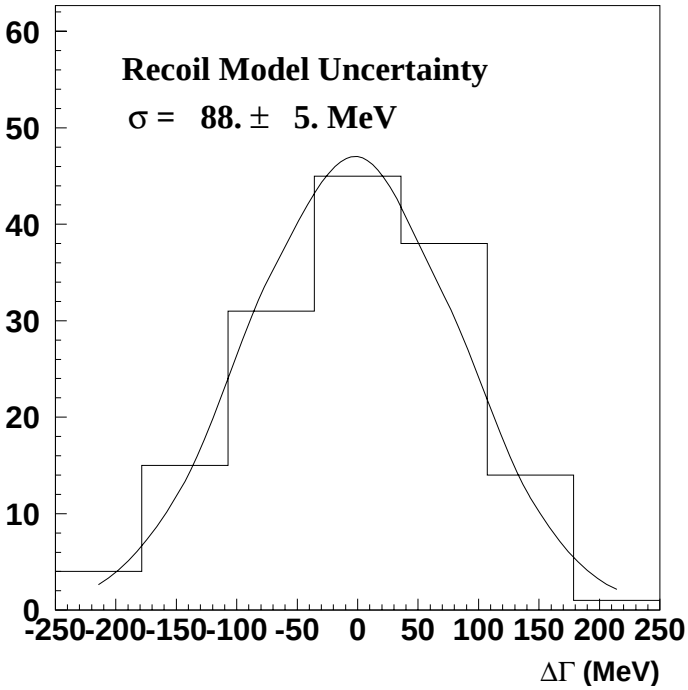

Figure 7.3

The variation in , (W) from the variation of the recoil transverse energy model parameters using the covariance matrix.

We extract , (W) from 50 million event Monte Carlo simulations for each PDF. The six , (W) values are listed in Table 7.1 and have a standard deviation of 16 MeV. Therefore we take the uncertainty of 16 MeV as the uncertainty in the W width from our choice of PDF.

7.7 Muon Identification and Removal

In selecting our data sample we used the criteria $E_{\rm CEM} < 2$ GeV and $E_{\rm CHA} < 6$ GeV to identify muons. The $E_{\rm CEM}$ cut was included in the Monte Carlo simulation, but both criteria should be studied as still being possible sources of bias in the W width measurement. Any possible bias will be related to the actual cut level we

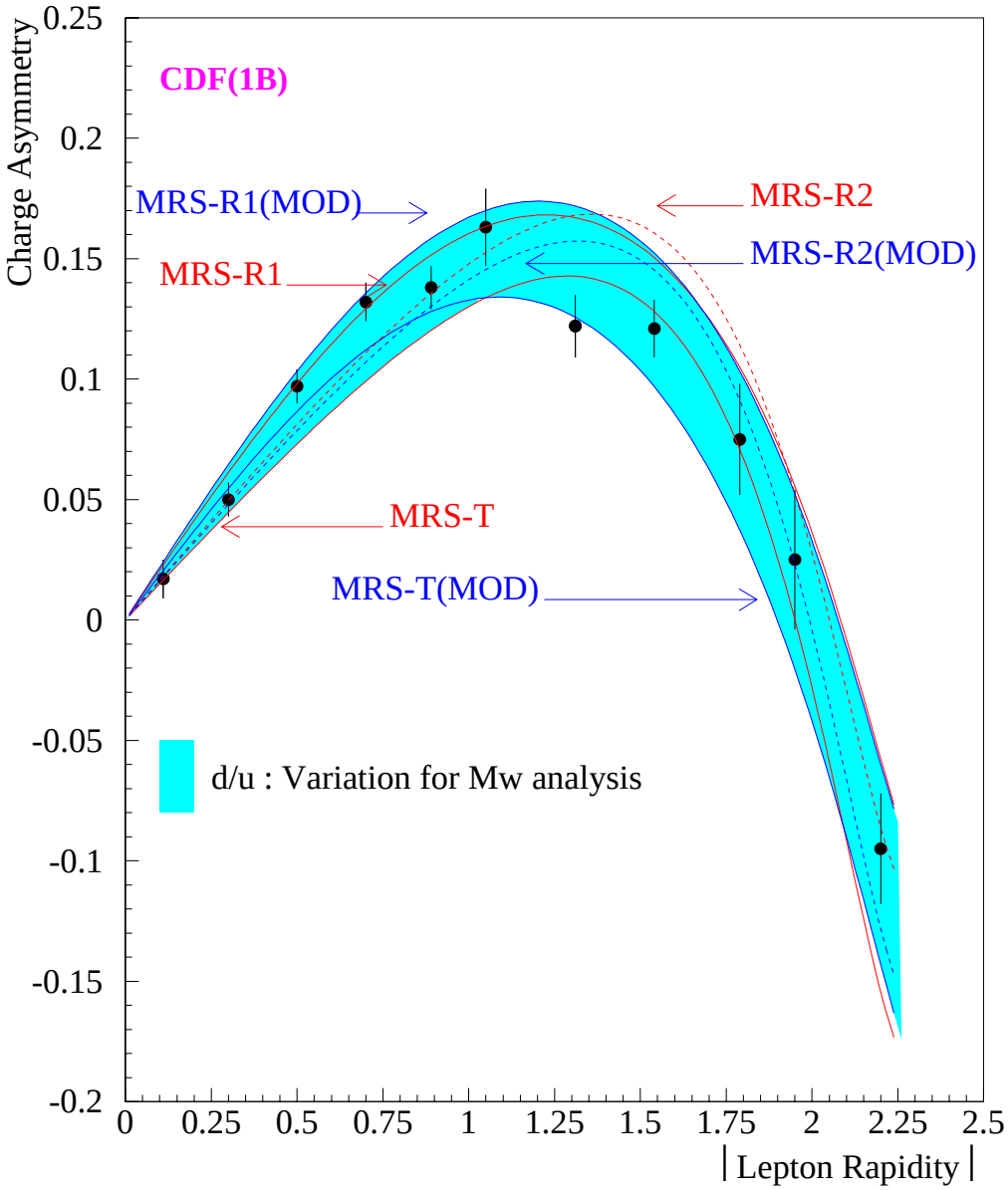

Figure 7.4

CDF W charge asymmetry measurements compared to the predictions of various parton distribution functions.

Table 7.1

W width for various PDF's.

PDF	, (W) (GeV)
MRS-R1	1.761
MRS-R1(MOD)	1.778
MRS-R2	1.791
MRS-R2(MOD)	1.779
MRS-T	1.769
MRS-T(MOD)	1.746

have chosen, so it is easiest to look for it by changing the cut levels of E_{CEM} and E_{CHA} in the data. The table of E_{CEM} cut variations (Table 7.2) shows a maximum variation of 17 MeV in , (W) the table of E_{CHA} cut variations (Table 7.3) shows a maximum variation of 34 MeV in , (W). We take the greater of the two variations, 34 MeV, to be the systematic uncertainty in , (W) due to the muon identification criteria.

7.8 Trigger

The most prominent effect of the triggers on the W data sample is in the η and ϕ distributions, as shown in figure 5.1. Having only one trigger instead of three would make these distributions flatter. Therefore we measure the effect of using flat η and ϕ distributions in the Monte Carlo simulation. A positive shift of 13

Table 7.2

Shifts in W width resulting from various $E_{\rm CEM}$ cuts.

Maximum $E_{\rm CEM}$ (GeV)	# of fit events	Δ, (MeV)
2.0	196	0.0
1.8	196	+7
1.6	195	+1
1.4	195	+17
1.2	192	+6
1.0	190	+7
0.8	186	+15

MeV in the W width is found and is used as the uncertainty in , $_W$ due to any possible trigger bias.

7.9 *W* Mass

In the Monte Carlo simulation, the W mass value used is the most current world average value. The world average of direct W mass measurements from D0, CDF, UA2, and LEP-2 is $M_W = 80.40 \pm 0.04$ GeV [34]. We randomly select 20 M_W values from a Gaussian distribution representing the world average measurement and generate a 50 million event Monte Carlo simulation for each value. Fitting each Monte Carlo simulation to our data, we obtain a standard deviation of 6 ± 2 MeV in the resulting , $_W$ values. We use this to be our uncertainty in , $_W$ from the W mass value used in the Monte Carlo simulation.

Table 7.3

Shifts in W width resulting from various $E_{\rm CHA}$ cuts.

Maximum $E_{\rm CHA}$ (GeV)	# of fit events	Δ, (MeV)
6.0	196	0.0
5.5	194	-17
5.0	193	-16
4.5	193	$+1$
4.0	189	-34

7.10 Radiative Corrections

The PHOTOS software package is used to generate up to two photons to represent the effect of QED radiative corrections. Setting PHOTOS to generate only a single photon at most, we find that $,_W$ has a positive shift of 8 MeV. An alternative algorithm based on the Berends and Kleiss calculation [35] generates up to one photon. Using this algorithm yields a negative shift in $,_W$ of 3 MeV. We use the maximum of these two variations and take the uncertainty in $,_W$ from radiative corrections to be 8 MeV.

7.11 Backgrounds

7.11.1 $Z \to \mu\mu$

The simulation of the $Z \to \mu(\mu)$ background was described in section 5.3.1. When included in the Monte Carlo simulation this background causes a shift of -67 MeV in the W width and an uncertainty of $\pm$31 (stat.) $\pm$5 (syst.) MeV. The

uncertainty in this shift has a statistical and a systematic uncertainty contribution. When we fluctuate the number of $Z \to \mu(\mu)$ background events in the fit region with Poisson statistics about the mean of 5 events we obtained in section 5.3.1, we obtain a statistical uncertainty of 31 MeV in , $_W$ when put into the Monte Carlo simulation. The systematic uncertainty in this shift is dominated by the accuracy of the track finding efficiency measurements and parton distribution functions used in the simulation. The track finding efficiencies have an estimated error of 10% [36] which lead to an uncertainty of 5 MeV in , $_W$ when included in the simulation. Six PDF's with a reasonable agreement with W asymmetry measurements in the $|\eta| <$ 1 region are presently known [21]. We use each PDF to produce a Z background distribution and it is found that the W width values measured have a standard deviation of 2 MeV, which we take as the uncertainty in , $_W$ due to the choice of PDF. Combining the statistical and systematic contributions, the total uncertainty in the W width from the $Z \to \mu(\mu)$ background is therefore 31 MeV.

7.11.2 $W \to \tau\nu$

In section 5.3.2 we found that the $W \to \tau\nu$ background consisted of 438 ± 21 events over the normalization region and $2 \pm \sqrt{2}$ events in the fit region. Inclusion of this background in the Monte Carlo simulation shifts the W width by $+25 \pm 24$ MeV, where the uncertainty is obtained from a sample of 200 $W \to \tau\nu \to \mu\nu\nu\nu$ fit-region transverse mass distributions generated from a Poisson distribution with a mean of 2 events.

7.11.3 Heavy-Flavor Decays and Fakes (QCD)

The QCD background was discussed in section 5.3.3. To find the shift and uncertainty in the W width from inclusion of the QCD background, the 4 events

in the $100 < M_T < 200$ GeV region are fluctuated with Poisson statistics, and a sample of 200 QCD background distributions is obtained. For each distribution, the shift in the W width value is obtained from the Monte Carlo simulation. The width is found to shift by -24 ± 28 MeV when the QCD background is added to the Monte Carlo simulation.

7.11.4 Cosmic Rays

In section 5.3.4 we found that 4 ± 2 ($\{0.018 \pm 0.009\}\%$) cosmic events were predicted for the cosmic ray background in the $50 < M_T < 100$ GeV/c^2 region. No cosmic ray events were found in the $100 < M_T < 200$ GeV/c^2 region after a scan. Inclusion of the cosmic ray background in the Monte Carlo simulation shifts the W width by -1 ± 1 MeV.

7.11.5 Summary

Table 7.4 summarizes the backgrounds and corresponding uncertainties in the W width. Overall, the presence of the backgrounds causes the W width to shift by -139 MeV. Combining the errors from each background in quadrature, the W width has an uncertainty of 48 MeV due to the backgrounds present.

Table 7.4

Background estimates and their effect on the W width measurement. Δ, is the shift in , $_W$ caused by inclusion of the background.

Decay	$50 < M_T < 200$ # events	$100 \leq M_T < 200$ GeV # events	Δ, (MeV) $\pm$(stat.)$\pm$(syst.)
Lost $Z \to \mu\mu$	761	5	$-67 \pm 31 \pm 5$
$W \to \tau\nu \to \mu\nu\nu\nu$	438	2	$+25 \pm 24 \pm$ negl.
QCD (dijet)	175	4	$-24 \pm 28 \pm$ negl.
Cosmic rays	4	0	$-1 \pm 1 \pm$ negl.
Total background	1378	11	-139 ± 48
Data sample	21791	196	
% Background	6%	6%	

8. CONCLUSION

A summary of the uncertainties in Γ_W is shown in Table 8.1. The overall systematic error in Γ_W is 135 MeV. Therefore we report as our directly measured W width for Run 1B in the muon channel, the value:

$$\boxed{\Gamma_W = 1.78^{+0.20}_{-0.19}(\text{stat.}) \pm 0.14(\text{syst.})\text{GeV}}$$

Table 8.1

Summary of uncertainties in the W width measurement (each rounded to the nearest 5 MeV)

Uncertainty	$\Delta_{,\,W}$ (MeV)
Recoil modeling	90
input p_T^W	70
Backgrounds	50
μ ID, trigger, detector model	40
μ resolution	20
p_T scale from $Z \to \mu\mu$	15
Parton distribution functions	15
Radiative corrections	10
W mass	10
Nonlinearity in p_T^μ scale	5
All systematics	135
Statistical	195
Total uncertainty	235

BIBLIOGRAPHY

BIBLIOGRAPHY

1. J.L. Rosner, M.P. Worah, and T. Takeuchi. *Phys. Rev. D*, **49**:254, 1994.

2. K. Einsweiler. CDF/ANAL/ELECTROWEAK/CDFR/3581. CDF Internal Note, 1996.

3. D. Karlen. Experimental Status of the Standard Model. 1998.

4. Particle Data Group. Review of particle physics. *Eur. Phys. J. C*, **3**:1, 1998.

5. Albajar et al. *Phys. Lett. B*, **253**:503, 1991.

6. Alitti et al. *Phys. Lett. B*, **276**:365, 1992.

7. F. Abe et al. *Phys. Rev. Lett.*, **74**:341, 1995.

8. F. Abe et al. *Phys. Rev. D*, **52**:2624, 1995.

9. Abachi et al. *Phys. Rev. Lett.*, **75**:1456, 1995.

10. Preliminary 1999 results from the D0 experiment at Fermilab given at the web site: `http://www-d0.fnal.gov/public/wz/xsection/xsection.html` .

11. M. Acciarri et al. *Phys. Lett. B*, **413**:176, 1997.

12. K. Ackerstaff et al. *Eur. Phys. J. C*, **1**:395, 1998.

13. Particle Data Group. *Phys. Rev. D*, **50**:1173, 1994.

14. V. D. Barger and R. J. N. Phillips. *Collider Physics*, volume **71** of *Frontiers in Physics*. Addison-Wesley, 1987.

15. P. Azzi et al. *Nucl. Instrum. Methods Phys. Res. A*, **360**:137, 1995.

16. G. Ascoli et al. *Nucl. Instrum. Methods Phys. Res. A*, **268**:33, 1988.

17. G. W. Foster et al. A Fast Hardware Track-Finder for the CDF Central Tracking Chamber. *Nucl. Instrum. Methods Phys. Res. A*, **269**:93, 1988.

18. Y.-K. Kim. CDF/ANAL/ELECTROWEAK/CDFR/4757. CDF Internal Note, 1998.

19. L. Nodulman. CDF/DOC/TRACKING/CDFR/4056. CDF Internal Note, 1997.

20. B. Ashmanskas, A. Mukherjee. CDF/DOC/TRACKING/PUBLIC/4456. CDF Internal Note, 1998.

21. M. Lancaster. CDF/ANAL/ELECTROWEAK/CDFR/4770. CDF Internal Note, 1998.

22. M. Lancaster. CDF/ANAL/ELECTROWEAK/CDFR/4046. CDF Internal Note, 1997.

23. A.D. Martin, R.G. Roberts, W.J. Stirling. *Phys. Lett. B*, **387**:419, 1996.

24. E. Barberio and Z. Was. *Comput. Phys. Comm.*, **79**:291, 1994.

25. E. Barberio, B. van Eijk, and Z. Was. *Comput. Phys. Comm.*, **66**:115, 1991.

26. P. B. Arnold and R. P. Kauffman. *Nucl. Phys. B*, **349**:381, 1991.

27. P. B. Arnold and M. Reno. *Nucl. Phys. B*, **319**:37, 1989.

28. P. B. Arnold, M. Reno, and R. K. Ellis. *Phys. Rev. D*, **912**:912, 1989.

29. W.T. Giele and S. Keller. *Phys. Rev. D*, **57**:4433, 1998.

30. Y.-K. Kim. CDF/ANAL/ELECTROWEAK/CDFR/4063. CDF Internal Note, 1997.

31. T.M. Liss and R. Roser and A. Martin. CDF/ANAL/TOP/CDFR/3931. CDF Internal Note, 1996.

32. D. Glenzinski and P. Schlabach. CDF/DOC/MUON/CDFR/2954. CDF Internal Note, 1995.

33. F. James. *Rep. Prog. Phys.*, **43**:1145, 1980.

34. Larry Nodulman. 17th International Workshop on weak Interactions and Neutrinos (WIN99), Cape Town, South Africa. January 1999.

35. J.P. Revol J.P. Vialle F.A. Berends, R. Kleiss. *Z. Phys C*, **27**:155, 1985.

36. K. Einsweiler and Y.-K. Kim. CDF/ANAL/ELECTROWEAK/CDFR/2400. CDF Internal Note, 1993.

VITA

VITA

Adam Hardman was born in Christchurch, New Zealand on December 18, 1965. He finished his high school education at Hamilton Boys High in Hamilton, New Zealand, in 1983. He attended the University of Waikato, New Zealand, and received a B.Sc. in Physics and Applied Mathematics in 1987. He then attended the University of Auckland, New Zealand, and did Masters degree level thesis research in theoretical nonlinear fiber optics with Professor Peter Drummond. He received an M.Sc. in Physics in 1989 from the University of Auckland. Beginning studies at Purdue University in 1992, he received an M.S. in physics in 1994. He joined the CDF collaboration at Fermilab as student of Professor Arthur Garfinkel in 1995.